

1 **Evaluation of the Tau-Omega Model over Bare and Wheat-Covered Flat and Periodic**

2 **Soil Surfaces at P- and L-band**

3 Xiaoji Shen^{a, *}, Jeffrey P. Walker^a, Nan Ye^a, Xiaoling Wu^a, Foad Brakhasi^a, Nithyapriya Boopathi^{a,b,c},
4 LiuJun Zhu^{a,d}, In-Young Yeo^e, Edward Kim^f, Yann Kerr^g, and Thomas Jackson^h

5
6 ^a*Department of Civil Engineering, Monash University, Clayton, Australia*

7 ^b*Center of Studies in Resources Engineering, IIT Bombay, Mumbai, India*

8 ^c*IITB-Monash Research Academy, Mumbai, India*

9 ^d*Yangtze Institute for Conservation and Development, Hohai University, Nanjing, China*

10 ^e*School of Engineering, The University of Newcastle, Callaghan, Australia*

11 ^f*NASA Goddard Space Flight Center, Greenbelt, USA*

12 ^g*Centre d'Etudes Spatiales de la Biosphère, Toulouse, France*

13 ^h*USDA ARS Hydrology and Remote Sensing Laboratory (Retired), Beltsville, USA*

14
15
16
17
18
19
20
21
22 *Revision submitted to Remote Sensing of Environment*

23 *Date: February 12, 2022*

24
25
26
27
28
29 **Corresponding author.*

30 *E-mail addresses: xiaoji.shen@monash.edu, xiaoji.shen@foxmail.com (X. Shen).*

31 **Abstract:**

32 It has been over ten years since the successful launch of the first-ever dedicated satellite
33 for global soil moisture monitoring; Soil Moisture and Ocean Salinity (SMOS). Looking
34 towards the future, P-band (0.3-1 GHz) is a promising technique to replace or enhance the L-
35 band (1.4 GHz) SMOS and SMAP (Soil Moisture Active Passive) missions because of an
36 expected reduction in roughness and vegetation impact, leading to an improved soil moisture
37 accuracy over rougher soil surfaces and more densely vegetated areas. Accordingly, this
38 investigation evaluated the tau-omega model at P-band (0.75 GHz) using a tower-based
39 experiment in Victoria, Australia, where brightness temperature observations were collected
40 concurrently at P- and L-band over bare and wheat-covered flat and periodic soil surfaces. The
41 potential to retrieve soil moisture without discriminating periodic and flat surfaces was
42 investigated by applying the roughness and vegetation parameters calibrated for flat soil to
43 retrieve the moisture of periodic soil. Results showed that P-band had a comparable RMSE
44 across different roughness configurations (variations less than $0.016 \text{ m}^3/\text{m}^3$) for both bare and
45 wheat-covered soil, while the L-band RMSE was only comparable for wheat-covered soil,
46 indicating that periodic surfaces did not need to be discriminated in such scenarios. Conversely,
47 a difference of $0.022 \text{ m}^3/\text{m}^3$ was observed for L-band with bare soil. A reduced vegetation
48 impact was also demonstrated at P-band, with an RMSE of $0.029 \text{ m}^3/\text{m}^3$ achieved when
49 completely ignoring the wheat existence with under $4\text{-kg}/\text{m}^2$ vegetation water content, whereas
50 at L-band the RMSE increased to $0.063 \text{ m}^3/\text{m}^3$. This study therefore paves the way for a

51 successful P-band radiometer mission for obtaining more accurate global soil moisture
52 information.

53 **Keywords:** P-band, passive microwave, soil moisture retrieval, roughness, vegetation

54 1 Introduction

55 The amount of water in the Earth's soil is around just 17,000 km³ (Oki and Kanae, 2006),
56 merely accounting for 0.05% of the total freshwater and 0.001% of the total water on/in the
57 Earth (Shiklomanov, 1993). However, this small amount of water plays a crucial role in the
58 Earth system because it nourishes vegetation, animals, and billions of humans. Moreover, soil
59 moisture (SM) is a key parameter in the hydrological cycle that influences infiltration, runoff,
60 and evapotranspiration (Seneviratne et al., 2010). Furthermore, it controls the division of the
61 available energy at the land surface into sensible and latent heat fluxes (Koster et al., 2004).

62 To meet the growing need for global soil moisture data in hydrology, precision agriculture,
63 drought, and flood forecasting, weather prediction, climate change, etc., the Soil Moisture and
64 Ocean Salinity (SMOS) satellite (Kerr et al., 2010) and the Soil Moisture Active Passive
65 (SMAP) satellite (Entekhabi et al., 2010) were launched in 2009 and 2015, respectively. Both
66 use L-band (1.4 GHz/21-cm wavelength) radiometers to measure the microwave emission from
67 the Earth in the form of brightness temperature (TB), which is a function of the emissivity and
68 physical temperature of the target. The emissivity of bare soil varies from approximately 0.5
69 for smooth and very wet soil to close to 1 for rough and very dry soil (Ulaby et al., 1982), being
70 the primary link between soil moisture and TB.

71 Soil roughness is well known to complicate the interpretation of microwave radiometer
72 data and reduce the sensitivity of TB to soil moisture (Choudhury et al., 1979; Newton and
73 Rouse, 1980). As a result, Wang and Choudhury (1981) developed a tractable semi-empirical
74 model (referred to as the HQN model) to simulate the random roughness impact, which is

75 currently being used in the SMOS (Kerr et al., 2019) and SMAP (O'Neill et al., 2021a)
76 algorithms. Compared to flat soil, periodic (e.g., sinusoidal) row structures, a common type of
77 soil tillage used for cultivation purposes, are less likely to be correctly modeled as a quasi-
78 specular surface with random roughness (Ulaby et al., 1986).

79 Apart from roughness, the vegetation canopy attenuates (absorbs and scatters) the soil
80 emission and adds its own contribution to the overall emission, resulting in a noticeable
81 reduction in the sensitivity of TB to soil moisture (Jackson et al., 1982). The tau-omega (τ - ω)
82 model proposed by Mo et al. (1982) models the TB response of vegetation-covered soil. Optical
83 depth τ and single scattering albedo ω characterize the vegetation extinction and scattering,
84 defined as $\tau = \int_0^h \kappa_e dx$ and $\omega = \kappa_s / \kappa_e$, respectively, where extinction coefficient κ_e is the
85 sum of absorption coefficient κ_a and scattering coefficient κ_s , and h is the canopy height. The
86 τ is directly proportional to the vegetation water content (VWC, in kg/m²) of the canopy, while
87 the ω primarily depends on the type of vegetation (Mo et al., 1982).

88 The tau-omega model is essentially a zero-order solution of the radiative transfer
89 equations where multiple scattering is neglected, with applicability and accuracy being widely
90 evaluated (Gao et al., 2018; Li et al., 2020). Many retrieval algorithms have been developed
91 based upon this practical model, e.g., the single channel algorithm (SCA, Jackson, 1993) and
92 the dual channel algorithm (DCA, Njoku and Li, 1999; Njoku et al., 2003) for SMAP, the L-
93 band microwave emission of the biosphere (L-MEB) model (Wigneron et al., 2007) for SMOS,
94 the land parameter retrieval model (LPRM, Owe et al., 2001), and the multi-temporal dual
95 channel algorithm (MT-DCA, Konings et al., 2016; Konings et al., 2017).

96 The advancement of satellite observations and retrieval algorithms has made global soil
97 moisture maps available every three days or less with satisfactory accuracy. For example,
98 according to an evaluation of the SMAP Level 2 Soil Moisture Passive (L2SMP) Version 8
99 using in-situ validation sites (O'Neill et al., 2021b), the SCA V-polarization (SCA-V) and the
100 DCA had the same best overall performance of $\sim 0.036 \text{ m}^3/\text{m}^3$ in unbiased root-mean-square
101 error (ubRMSE), fulfilling the $0.04\text{-m}^3/\text{m}^3$ target accuracy of SMAP. However, the DCA
102 showed better ubRMSE than the SCA at two agricultural sites. Consequently, the DCA has
103 been adopted as the SMAP baseline algorithm since October 2021 (O'Neill et al., 2021a), with
104 the SCA-V having been the baseline algorithm from the launch of SMAP (Chan et al., 2016).

105 Despite the above-mentioned achievements, global soil moisture sensing is still facing a
106 few challenges. First, the moisture retrieval depth of the current L-band missions is believed to
107 be 5 cm or even shallower (Escorihuela et al., 2010; Liu et al., 2012; Zheng et al., 2019), which
108 limits direct application of the data in disciplines that require deeper soil moisture information,
109 e.g., weather prediction and climate research. Second, the accuracy of these satellite products
110 varies for different land surfaces. As an example, although the SMAP radiometer-based soil
111 moisture data meets its overall target accuracy, errors for croplands are considerably larger
112 (Chan et al., 2016; Colliander et al., 2017; Walker et al., 2019). Third, current SMAP and
113 SMOS algorithms do not specifically consider any correction of the periodic row structure
114 because of the lack of global information on temporally varying row shape, height, and
115 orientation. In addition, there is currently no basis for how to upscale such field information to
116 satellite footprint scales.

117 P-band (0.3-1 GHz/100-30-cm wavelength) is a promising candidate for conquering some
118 of the difficulties faced at L-band due to its longer wavelength. It is a widely held understanding
119 that a longer waveband should have a deeper moisture retrieval depth and reduced impact from
120 surface roughness and vegetation (Ulaby et al., 1986), resulting in a more useful contributing
121 depth and an overall higher soil moisture retrieval accuracy over vegetated rough/periodic soil
122 surfaces. Accordingly, a recent P-band radar study known as the Airborne Microwave
123 Observatory of Subcanopy and Subsurface (AirMOSS), has been conducted for retrieving root-
124 zone soil moisture and moisture profiles (Tabatabaenejad et al., 2014; Crow et al., 2018;
125 Tabatabaenejad et al., 2020). Alemohammad et al. (2019) concurrently collected P- and L-
126 band backscatter observations using AirMOSS and the NASA/JPL's Uninhabited Aerial
127 Vehicle SAR (UAVSAR), respectively, and demonstrated reduced vegetation scattering at P-
128 band. In addition, P-band satellite signals of opportunity has been proven to have a potential
129 for sensing subsurface soil moisture (Yueh et al., 2020). These findings have motivated a
130 spaceborne P-band-radar mission for mapping global forest biomass, i.e., Biomass (Le Toan et
131 al., 2011) scheduled for launch in 2023, and the SigNals of Opportunity: P-band Investigation
132 (SNoOPI) for soil moisture mapping scheduled for launch in early 2022 (Garrison et al., 2021).

133 In terms of microwave radiometry, no observational evidence has been reported to
134 demonstrate the postulated benefits of using P-band TB observations until the P-band
135 Radiometer Inferred Soil Moisture (PRISM, see <https://www.prism.monash.edu>) project of
136 Monash University. This project comprises a long-term tower experiment (2017-2021) and
137 four airborne campaigns (2017, 2018, 2019, and 2021) to concurrently collect P- and L-band

138 TB measurements over a range of roughness and vegetation conditions for investigating the
139 potentially superior capability of a P-band radiometer over an L-band radiometer for soil
140 moisture sensing. Taking advantage of the PRISM tower-based dataset, Shen et al. (2021) and
141 Shen et al. (2022) have demonstrated a larger moisture retrieval depth and a reduced roughness
142 impact at P-band compared to L-band over bare soil.

143 Following Shen et al. (2021) and Shen et al. (2022), this paper extends the investigation
144 to wheat-covered soil with flat and periodic surfaces. For the first time, the tau-omega model
145 was implemented at P-band to evaluate the vegetation effects at P- and L-band by comparing
146 the retrieval errors before and after accounting for the wheat canopy in the forward model.
147 Furthermore, the possibility of retrieving soil moisture over bare and wheat-covered soil
148 without discriminating periodic and flat surfaces was investigated, by applying the roughness
149 and vegetation parameters calibrated in flat soil to retrieve the soil moisture of periodic soil
150 with the SMAP SCA and DCA. This demonstration suggests that an improved global soil
151 moisture dataset may be possible using the longer wavelength P-band observations, even if the
152 same algorithms as those of SMAP are used.

153 **2 Experimental data**

154 A tower-based site was established at Cora Lynn, Victoria, Australia (Fig. 1a) from
 155 October 2017 to May 2021, to investigate the potential of P-band radiometry in soil moisture
 156 remote sensing. The field was 160 m by 160 m in size and divided into four quadrants (Q1-Q4
 157 from the northwest clockwise). A ten-meter-high tower was located at the center of the paddock
 158 (Fig. 1b), on which the two radiometers were installed, namely the Polarimetric P-band Multi-
 159 beam Radiometer (PPMR, Fig 1d) and the Polarimetric L-band Multi-beam Radiometer
 160 (PLMR, Fig. 1e). The PPMR and PLMR on the tower were rotated and tilted on a schedule so
 161 that they alternately observed the four quadrants at a variety of incidence angles (Fig. 1c).

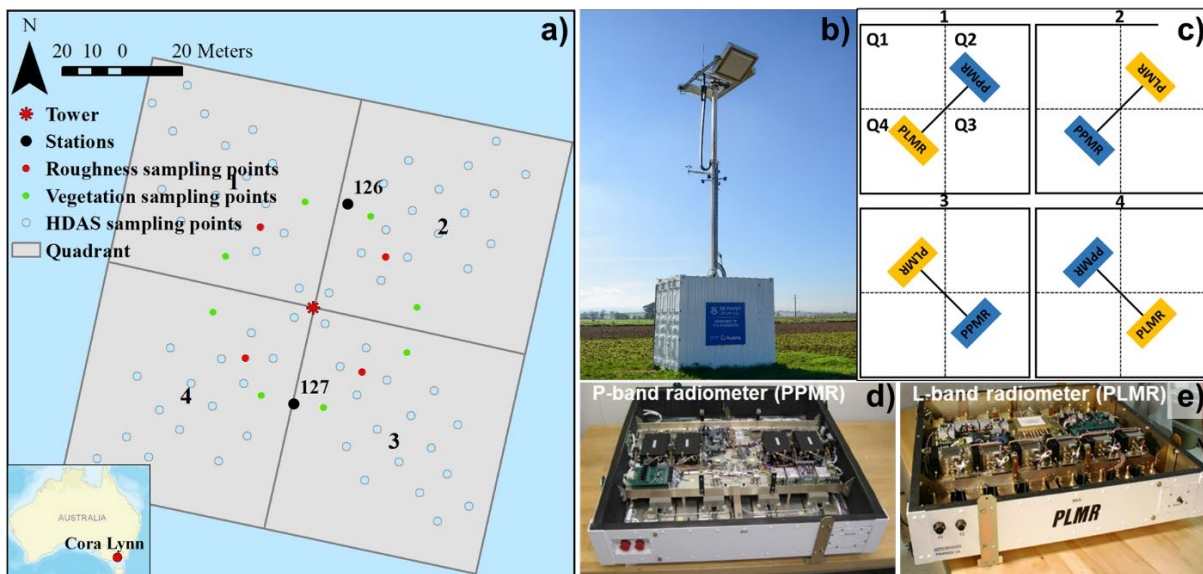


Fig. 1 Illustrations of the tower-based experiment at Cora Lynn, Victoria, Australia, including
 a) location map of the site; b) the tower carrying PPMR and PLMR; c) the four-step tower
 rotation cycle; d) PPMR operating at 0.742-0.752 GHz; and e) PLMR operating at 1.401-1.425
 GHz.

162 PPMR and PLMR operate at dual linear (horizontal (H) and vertical (V)) polarizations
 163 (H- and V-pol), with 30° and 15° beamwidth, respectively. For a 40° incidence angle, the
 164 spatial resolution of the 3-dB footprints of PPMR and PLMR were approximately 8.2×7.0 m
 165 and 4.0×4.0 m, respectively. Both PPMR and PLMR have a calibration accuracy of better
 166 than 1.5 K; please refer to Shen et al. (2021) for more details about PPMR and PLMR. Unless
 167 otherwise noted, the terms "P-band" and "L-band" hereafter refer to the frequencies at which
 168 PPMR and PLMR operate.

169 Stations 126 and 127 (Figs. 1a and 2a) continuously recorded soil moisture and
 170 temperature at 5-cm intervals down to 60 cm, as shown in Fig. 2b. The top probe was installed

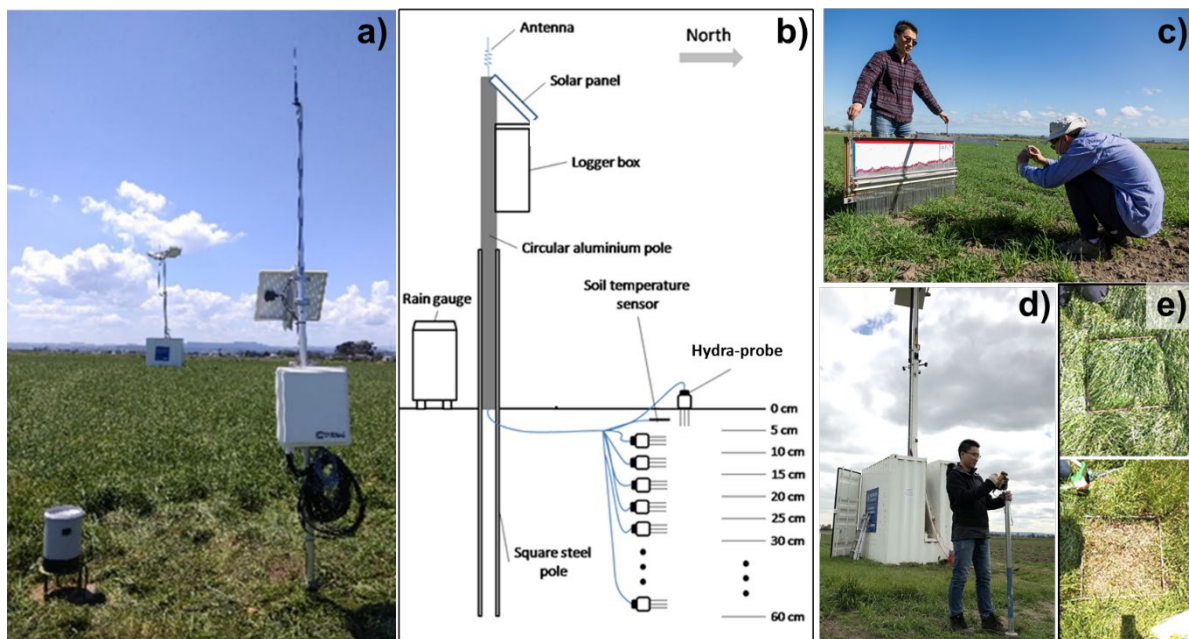


Fig. 2 Illustrations of the ground measurements, including a) station 126 monitoring soil moisture, temperature, and rainfall evolution; b) a diagram showing the station installation; c) soil surface roughness measurement with the pin-profiler; d) surface soil moisture measurement using HDAS; and e) an example of vegetation destructive sampling.

171 vertically from the surface, while the others were installed horizontally (Fig. 2b). Fig. 2d shows
172 how the spatial surface soil moisture (top ~5 cm) was measured at the locations shown in Fig.
173 1a using a system developed in-house, known as the Hydra-probe Data Acquisition System
174 (HDAS, Merlin et al., 2007). These HDAS measurements were not used in the formal analysis
175 but were used for checking the homogeneity of the soil moisture across the field and the
176 representativeness of the stations. The hydra-probes used in this study were calibrated
177 according to Merlin et al. (2007) and checked on-site using gravimetric samples. Soil texture
178 samples obtained across the field were found to be a silt loam with 18.0% clay, 10.9% sand,
179 and 71.1% silt. The soil bulk density of the surface soil layer in this site was 0.87 kg/m³.

180 Quadrants 1-4 were plowed with varied roughness structures for the wheat-growing cycle
 181 from July to December 2019 to compare the random roughness of flat soil and the periodic
 182 roughness of furrowed soil (Fig. 3). Table 1 shows the roughness measurements taken during
 183 the whole wheat-growing period. On each sampling day, a pin-profiler with an ~0.5-cm pin
 184 interval was used to take three consecutive 1-m measurements (totaling 3-m) in two
 185 perpendicular directions in each quadrant (Fig. 2c). These roughness measurements were not
 186 used in the formal analysis but to support that the roughness parameters can be assumed
 187 constant over the entire study period.

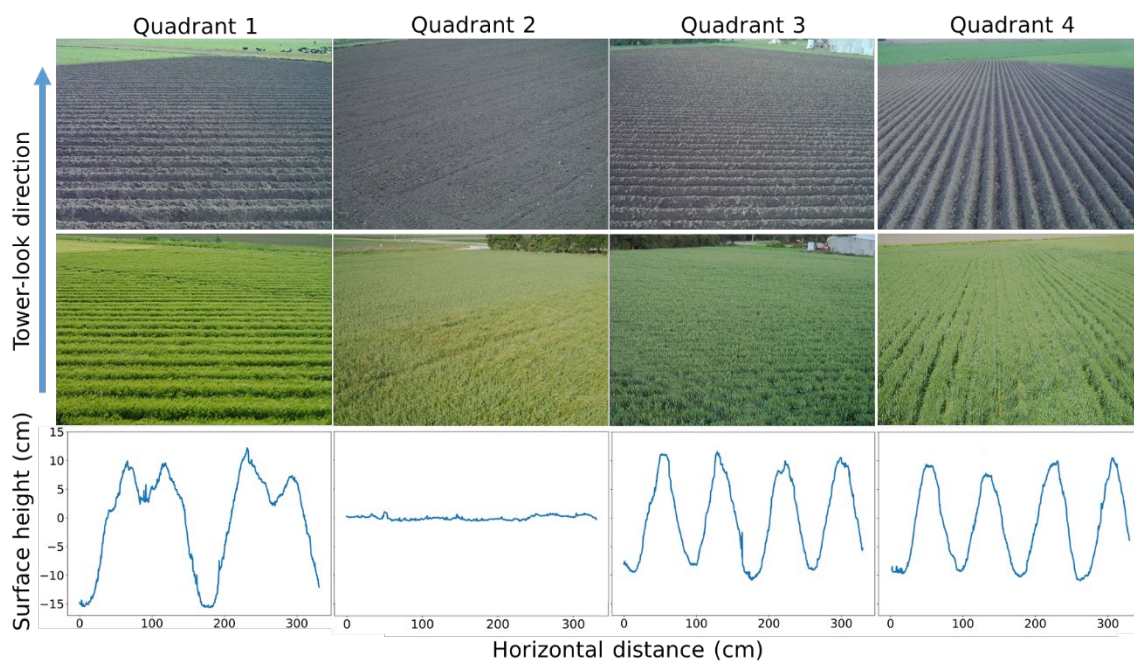


Fig. 3 Photos before the germination (top row) and at the maturity (middle row) of wheat, and diagrams of soil surface profiles (bottom row) of the four quadrants for the data used in this paper. Quadrants 3 and 4 were plowed in one pass and had the same roughness structures but with different orientations (perpendicular and parallel, respectively) relative to the tower look direction.

Table 1 Characterization of the roughness in the four quadrants.

Quadrant	Row structure	Periodic roughness			Random roughness			
		No. of profiles	Azimuth (°)	Period (cm)	Amplitude (cm)	No. of profiles	RMS height (cm)	Correlation length (cm)
1	Sinusoidal bench	6	90	165	10.5 ± 1.3	6	1.1 ± 0.5	9.2 ± 4.3
2	Flat	-	-	-	-	16	0.9 ± 0.2	9.5 ± 2.7
3	Sinusoidal	7	90	80	9.8 ± 1.2	7	0.8 ± 0.3	9.0 ± 4.2
4	Sinusoidal	7	0			7		

Azimuth is the angle between the radiometer look direction and the row direction; period is the row spacing; and amplitude is half of the vertical distance between the bottom and the top of the row. For the periodic soil in Q1, Q3, and Q4, the roughness measurements across the rows were used to calculate the “periodic roughness” in the table, while those along the rows were used to calculate the “random roughness” in the table. For Q2, the measurements in two perpendicular directions were averaged to calculate the roughness statistics. Q3 and Q4 were plowed in one pass and had the same roughness structure (just different orientations relative to the tower look direction), and therefore the measurements in these two quadrants were averaged.

188 In this study, two periods in the entire wheat-growing cycle were used: 1) the bare soil
189 period from July 17 to 31, 2019, before wheat germination (Fig. 3; top row) - details of this
190 were presented by Shen et al. (2022); and 2) the wheat-covered soil period (Fig. 3; middle row)
191 from November 13 to December 21, 2019, when matured wheat was senescing (a data example
192 is plotted in Fig. 4). The current study used the daily TB observations at 40° incidence angle
193 for P-band and at 38° incidence angle for L-band (Fig. 4a), in order to approximate the fixed
194 40° incidence angle of SMAP (Entekhabi et al., 2014). Moreover, Zhao et al. (2020) provide
195 support by showing that 40° to 45° provided the best retrieval accuracy. Each of the TB
196 observations in Fig. 4a was averaged from approximately 300 readings collected over a five-
197 minute interval at around 6 am, because the soil temperature and dielectric profiles are likely
198 to be more uniform at 6 am than other times of the day (Basharinov and Shutko, 1975). In

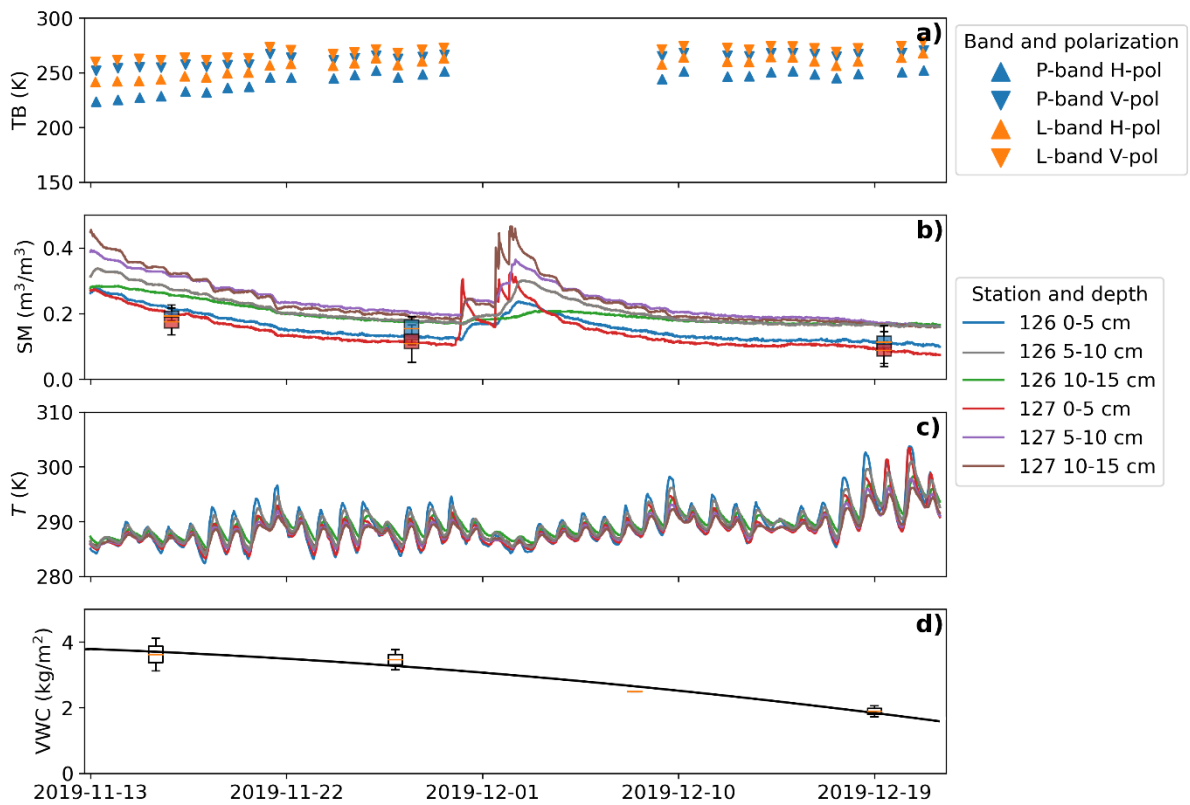


Fig. 4 Collected data including a) TB observations at 6 am in Q1 as an example, with the data gaps resulting from the tower being lowered due to high wind on those days; b) station time-series soil moisture with HDAS measurements (boxplots); c) station time-series soil temperature; and d) observed (boxplots) with fitted (black line) vegetation water content in Q1 as an example. For clarity only the data collected from the top 3 sensors are plotted in b) and c). Corresponding to the soil moisture evolutions of station 126 (in blue) in Q2 and station 127 (in red) in Q1, 3 and 4, the blue and red boxplots in b) show the maximum, 75% percentile, median, 25% percentile, and minimum of the spatial HDAS measurements in Q2 as well as Q1, 3 and 4, respectively.

199 addition, the difference between soil and canopy temperature is also minimized (Entekhabi et
 200 al., 2014).

201 Figs. 4b and c show the time series of soil moisture and temperature, respectively,
202 collected from stations 126 and 127. This investigation follows the precedent of Shen et al.
203 (2022) by using station 126 as the reference in Q2 and station 127 as the reference for Q1, Q3,
204 and Q4 based on the agreement between HDAS measurements and the station soil moisture in
205 flat and periodic quadrants respectively (Fig. 4b). The station observations were considered
206 representative of the radiometer footprints because the HDAS measurements were relatively
207 uniform across each quadrant and agreed with the corresponding station measurements (Fig.
208 4b). The destructive vegetation samples were taken weekly (Fig. 2e) at the locations shown in
209 Fig. 1a. Accordingly, Fig. 4d presents the VWC measurements as boxplots and a fitted
210 quadratic polynomial function to represent the VWC evolution.

211 While P-band was found to have a greater moisture retrieval depth (~ 7 cm) than L-band
212 (~ 5 cm) over bare soil (Shen et al., 2021), given the difficulty in continuously measuring soil
213 moisture at 5-7-cm depths, and the highly correlated soil moisture between neighboring layers,
214 the daily mean soil moisture at around 6 am in the 0-5-cm layer from the station (Fig. 4b) was
215 used for both P- and L-band evaluation in this paper.

216 **3 Forward model**

217 The well-known tau-omega model (Mo et al., 1982) characterizes the brightness
218 temperature of the thermal emission (TB_p , where subscript P denotes either H- or V-pol) from
219 a vegetated soil surface with four terms, i.e., 1) the direct upward emission from vegetation
220 (TB_p^{V-up}); 2) the downward vegetation emission reflected by the soil and attenuated by the

221 canopy layer ($TB_p^{v\text{-down}}$); 3) the upward soil emission attenuated by the canopy layer (TB_p^s),
 222 and 4) the downwelling sky emission ($TB^{\text{sky-down}}$) reflected by the soil and attenuated twice
 223 by the canopy layer (TB_p^{sky}), formulated as (Ulaby et al., 2014)

$$224 \quad TB_p = TB_p^{v\text{-up}} + TB_p^{v\text{-down}} + TB_p^s + TB_p^{\text{sky}} = (1 - \omega)(1 - \gamma_p)T_{\text{eff}}^v + (1 - \omega)(1 - \gamma_p)\gamma_p\Gamma_p T_{\text{eff}}^v + (1 - \Gamma_p)\gamma_p T_{\text{eff}}^s + TB^{\text{sky-down}}\Gamma_p\gamma_p^2, \quad (1)$$

226 where γ_p and T_{eff}^v are the transmissivity and effective temperature of the vegetation canopy,
 227 and Γ_p and T_{eff}^s are the reflectivity and effective temperature of the soil. The T_{eff}^v was assumed
 228 to be equal to the physical soil temperature in the 0-5-cm layer because the difference between
 229 canopy and soil temperature is minimal at 6 am (Fagerlund et al., 1970). Moreover, $TB^{\text{sky-down}}$
 230 was assumed to be constant and calculated to be 13.9 K at P-band and 5.3 K at L-band (ITU,
 231 2015). The γ_p was computed from the optical depth τ_p using Beer's law such that

$$232 \quad \gamma_p = \exp\left[-\frac{\tau_p}{\cos(\theta)}\right]. \quad (2)$$

233 For bare soil, Eq. 1 can be simplified to

$$234 \quad TB_p = TB_p^s + TB_p^{\text{sky}} = (1 - \Gamma_p)T_{\text{eff}}^s + TB^{\text{sky-down}}\Gamma_p, \quad (3)$$

235 where Γ_p can be computed using the HQN model (Choudhury et al., 1979; Wang and
 236 Choudhury, 1981; Prigent et al., 2000)

$$237 \quad \Gamma_p = [(1 - Q_R)\Gamma_p^* + Q_R\Gamma_Q^*] \exp[-H_{RP}\cos^{N_{RP}}(\theta)], \quad (4)$$

238 where Γ_p^* is the specular reflectivity calculated from the Fresnel equations as a function of the
 239 relative soil dielectric constant ϵ_r ($\epsilon_r = \epsilon_r' - j\epsilon_r''$), including real (') and imaginary (") parts,
 240 such that

241
$$\Gamma_H^* = \left| \frac{\cos(\theta) - \sqrt{\varepsilon_r - \sin^2(\theta)}}{\cos(\theta) + \sqrt{\varepsilon_r - \sin^2(\theta)}} \right|^2 \quad (5)$$

242
$$\Gamma_V^* = \left| \frac{\varepsilon_r \cos(\theta) - \sqrt{\varepsilon_r - \sin^2(\theta)}}{\varepsilon_r \cos(\theta) + \sqrt{\varepsilon_r - \sin^2(\theta)}} \right|^2. \quad (6)$$

243 The dielectric constant was related to soil moisture in this paper by the model of Mironov et al.
 244 (2013b), given that it accounts for the interfacial (Maxwell-Wagner) relaxation of soil water at
 245 P-band. This model neglects temperature dependence on the dielectric constant by assuming a
 246 constant temperature of 20 °C. Since the soil temperature was close to 20 °C at 6 am for most
 247 days of the study period (Fig. 4c), and that the dielectric constant of moist soil does not change
 248 substantially from 10 to 30 °C (Wagner et al., 2011), it is believed that using this model was
 249 reasonable for this research rather than the one developed specifically for SMOS at L-band
 250 (Mironov et al., 2013a). In this current investigation, the daily mean soil moisture at around 6
 251 am in the 0-5-cm layer from the station (Fig. 4b) was used to simulate TB and evaluate the
 252 retrieved soil moisture at both P- and L-band.

253 According to radiative transfer theory, T_{eff}^S can be computed as (Choudhury et al., 1982)

254
$$T_{\text{eff}}^S = \int_0^\infty T(z) \alpha(z) \exp\left[-\int_0^z \alpha(z') dz'\right] dz, \quad (7)$$

255 where $T(z)$ is the soil temperature at depth z , and $\alpha(z)$ is the power absorption coefficient
 256 depending on the soil dielectric constant ε_r and the observation wavelength λ written as (Ulaby
 257 et al., 1986)

258
$$\alpha(z) = 2 \cdot (2\pi/\lambda) \cdot \left| \text{Im}\left[\sqrt{\varepsilon_r(z)}\right] \right|, \quad (8)$$

259 where $\text{Im}[\]$ represents the imaginary part. In this paper, the effective soil temperature was
 260 calculated using Eqs. 7 and 8, as well as the soil moisture and temperature measurements. The

261 soil was modeled as a semi-infinite medium, with the soil moisture and temperature below 60
262 cm assumed to be the same as those observed in the 55-60-cm layer.

263 **4 Methodology**

264 Given that the same mono-angular configuration as SMAP ($\sim 40^\circ$) was adopted in this
265 research, the SMAP SCA and DCA approaches were implemented to evaluate the tau-omega
266 model over bare and wheat-covered flat and periodic soil surfaces at P- and L-band. Additional
267 to applying the default SMAP parameters to the soil moisture retrieval, roughness and
268 vegetation parameters were locally calibrated in Q1-Q4 by feeding the forward model with
269 coincident TB and soil moisture measurements. Subsequently, the calibrated parameters over
270 the flat soil (Q2) were applied to the soil moisture retrieval over the periodic soil surfaces (Q1,
271 Q3 and Q4), taking Q2 as calibration data and Q1, Q3 and Q4 as validation data. Finally, the
272 retrieval performance for Q1, Q3 and Q4 was compared to Q2 as a benchmark.

273 Roughness and vegetation parameters can compensate for each other and thus cannot be
274 calibrated together to achieve a robust result (Njoku and Chan, 2006; Patton and Hornbuckle,
275 2012; Martens et al., 2015). To disentangle roughness and vegetation effects, Wigneron et al.
276 (1995) separately calibrated roughness and vegetation parameters by using the data before and
277 after the vegetation canopy development, respectively. A similar methodology was also
278 employed in this research. The roughness parameters calibrated over the bare soil period were
279 therefore applied to the wheat-covered soil period because the surface roughness was found to

Table 2 The default SMAP SCA parameters for croplands (O'Neill et al., 2021a).

Parameter	Value
H_R	0.108
Q_R	0
N_{RP}	2
b	0.11
ω	0.05

280 have little change throughout the entire period, as indicated by the small standard deviation in
 281 Table 1.

282 4.1 SCA

283 The SCA (Jackson, 1993) retrieves soil moisture using the TB observation at either H- or
 284 V-pol with all roughness and vegetation parameters known (Table 2). The b in Table 2 is an
 285 empirical parameter that builds a linear relationship between τ and VWC (Jackson and
 286 Schmugge, 1991), and thus τ can be estimated from

$$287 \quad \tau = b \cdot \text{VWC}. \quad (9)$$

288 As in the SMAP SCA (O'Neill et al., 2021a), this research assumed the parameters in Table 2
 289 were invariant throughout the study period.

290 Inversion of the forward model used the SLSQP (Sequential Least Squares Programming,
 291 Kraft, 1988) algorithm to iteratively minimize a cost function (CF) computed from the
 292 differences between the observed TB (TB_p^{obs}) and the simulated TB (TB_p) at either H- or V-
 293 pol, expressed as

$$294 \quad \text{CF} = (\text{TB}_p^{\text{obs}} - \text{TB}_p)^2. \quad (10)$$

295 The initial value of soil moisture was set to zero to avoid any potentially misleading prior
296 knowledge in the retrieval. A bound of 0-1 m³/m³ was imposed on the retrieved soil moisture
297 to ensure reasonable values were obtained.

298 4.2 DCA

299 The DCA (Njoku and Li, 1999; Njoku et al., 2003) uses dual-pol TB observations to
300 retrieve two parameters. Unlike the SCA, the SMAP DCA uses a global map of H_R to
301 concurrently retrieve soil moisture and τ . The H_R values vary from pixel to pixel, so no specific
302 H_R value can be referred to in this paper. In addition, while N_{RP} is assumed to be 2 as in the
303 SCA, Q_R is no longer assumed to be a constant value. Accordingly, H_R and Q_R were calibrated
304 locally in Q1-Q4 using the bare soil data prior to undertaking retrieval. Afterward, soil moisture
305 and τ were concurrently retrieved using the dataset for the wheat-covered period and the
306 calibrated H_R and Q_R in Q2. The ω was assumed to be the same as in the SMAP DCA for both
307 P- and L-band, being 0.6.

308 The CF minimized by the SLSQP algorithm using dual-pol TB at $\sim 40^\circ$ incidence angle
309 during the retrieval period was

$$310 \quad CF = (TB_H^{\text{obs}} - TB_H)^2 + (TB_V^{\text{obs}} - TB_V)^2 + \frac{(\tau^{\text{ini}} - \tau)^2}{\sigma(\tau)^2}, \quad (11)$$

311 where τ^{ini} and τ are the initial and retrieved values of the optical depth, and $\sigma(\tau)$ is the
312 parameter to balance the weight of the retrieved parameters for the optimization process to
313 converge. The initial values of soil moisture and τ were set to zero. The same $\sigma(\tau)$ value as in
314 the SMAP DCA was adopted, i.e., 0.05 (O'Neill et al., 2021a).

315 **5 Results**

316 **5.1 SCA – the HQN model for bare soil**

317 Since Shen et al. (2022) found that the default SMAP parameters cannot fully account for
 318 the periodic roughness impact, especially at L-band, the H_R values were calibrated using the
 319 bare soil data (Fig. 5). A range of H_R values were used to simulate the TB for P- and L-band
 320 and H- and V-pol respectively using the bare soil model (Eq. 3). The H_R values that produced

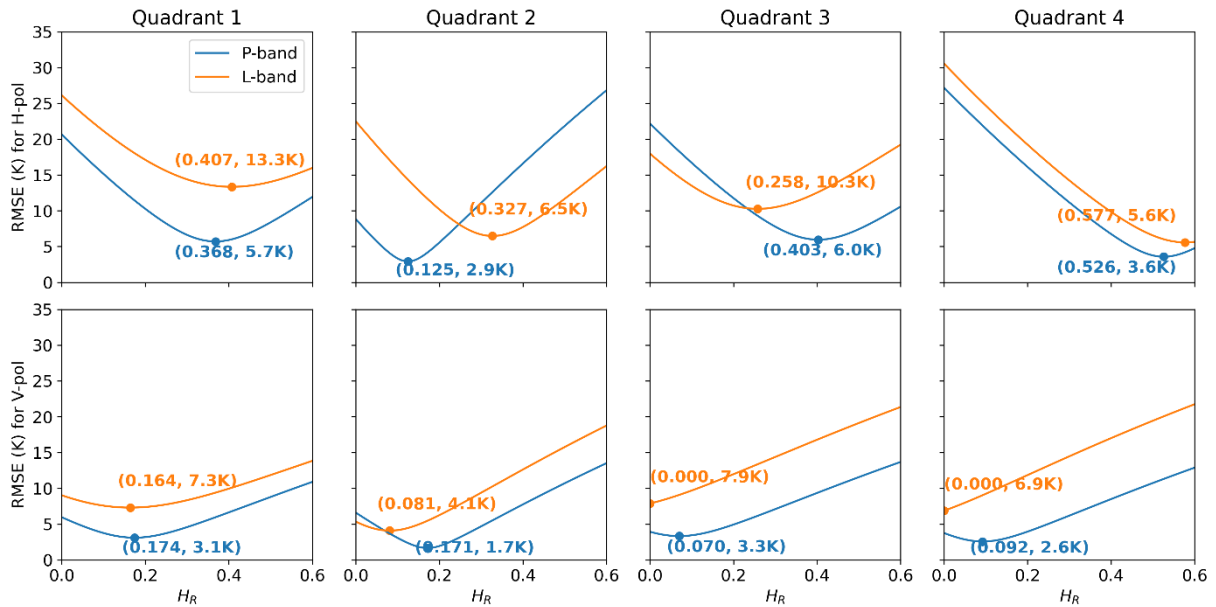


Fig. 5 RMSE (K) between the observed and simulated TB using a range of H_R values at H-pol (top row) and V-pol (bottom row) over the bare soil in each quadrant. The model for bare soil (Eq. 3) was adopted as the forward model. The dots with values indicate the minimum RMSE and the corresponding H_R values for P-band (in blue) and L-band (in orange). The parameters Q_R and N_{RP} were assumed to be the same as in the SMAP SCA at both P- and L-band, being 0 and 2, respectively.

321 the minimum RMSE between the simulated and observed TB were considered the optimum,
 322 marked as the dots with annotated values in Fig. 5.

323 Compared to L-band, the HQN model performed better at P-band based on its lower
 324 RMSE. For example, the minimum RMSE in Q1 and Q3 was no higher than 6 K at P-band,
 325 while that at L-band was higher than 10 K. Moreover, at L-band V-pol, the RMSE in Q3 and
 326 Q4 was a minimum at $H_R = 0$ and will further decrease if negative H_R is allowed. These
 327 phenomena can be attributed to the substantial impact of periodic row structures and the

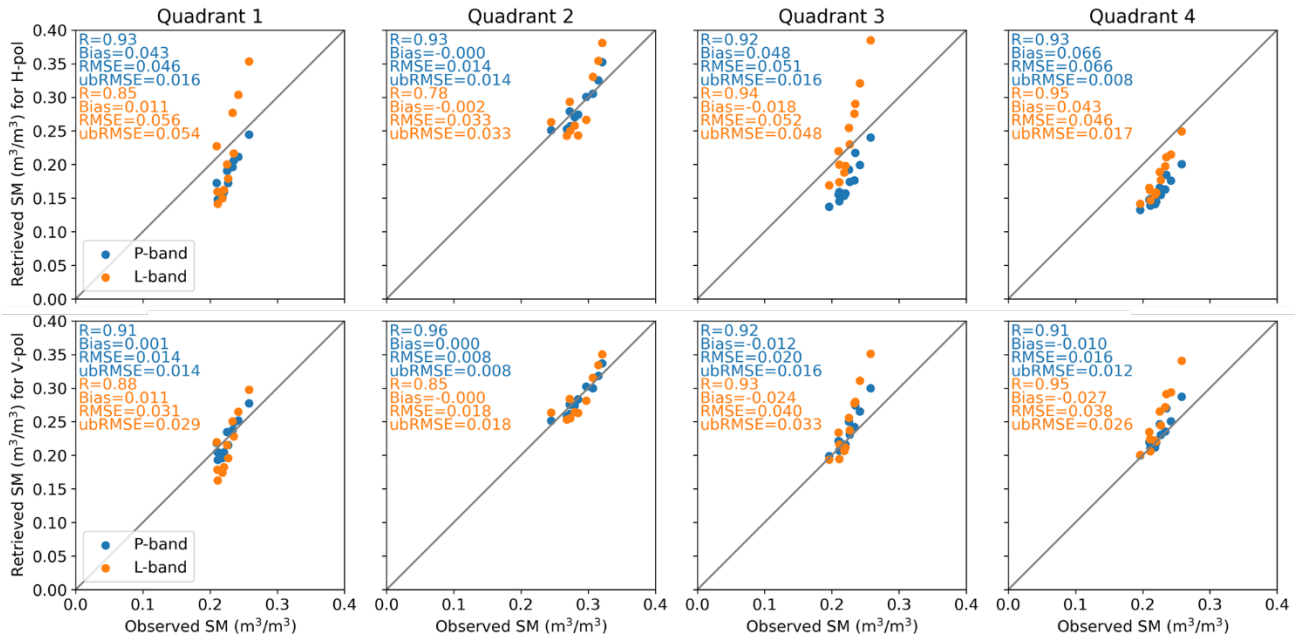


Fig. 6 Retrieved versus observed soil moisture for H-pol (top row) and V-pol (bottom row) over the bare soil in each quadrant, using the SCA (Eq. 10) with the bare soil forward model (Eq. 3). Calibrated H_R values from the period of bare flat soil in Q2 were used for all quadrants here, i.e., 0.125 and 0.171 for P-band H- and V-pol, respectively, and 0.327 and 0.081 for L-band H- and V-pol, respectively. The parameters Q_R and N_{RP} were assumed to be the same as those from the SMAP SCA at both P- and L-band, being 0 and 2, respectively.

328 inapplicability of the SMAP SCA configuration (i.e., $Q_R = 0$ and $N_{RV} = 2$) for periodic
329 roughness at L-band. For both P- and L-band and both H- and V-pol, Q2 had the lowest
330 calibration residual across the four quadrants with only one exception (L-band H-pol in Q4),
331 indicating the more considerable roughness impact of periodic surfaces than from the flat
332 surface in Q2. Importantly, the H_R in the four quadrants was more comparable at P- than L-
333 band at V-pol, with the standard deviation being 0.046 and 0.068, respectively.

334 To evaluate the induced retrieval error from applying the calibrated H_R in flat soil to
335 periodic soil, the optimal parameters calibrated in Q2 (Fig. 5) were used to retrieve the soil
336 moisture in all four quadrants for both bands and both polarizations, with the comparison of
337 the retrieved and observed soil moisture plotted in Fig. 6. As expected, Q2 was seen to have
338 the best retrieval performance across all four quadrants because H_R was calibrated in Q2, which
339 was done intentionally to get a benchmark accuracy that can be compared to for the other three
340 quadrants with periodic soil surfaces. P-band was found to perform better than L-band in
341 RMSE in all quadrants except Q4 for H-pol. In Fig. 6, V-pol had better retrieval accuracy than
342 H-pol at both P- and L-band. Focusing on V-pol (Fig. 6 bottom row), P-band had similar
343 RMSEs across all four quadrants, whereas L-band showed higher RMSE over periodic soil
344 ($0.031\text{-}0.040\text{ m}^3/\text{m}^3$) than that over flat soil ($0.018\text{ m}^3/\text{m}^3$), indicating the reduced roughness
345 impact at P-band.

346 **5.2 SCA – the tau-omega model for wheat-covered soil**

347 The default SMAP SCA parameters for croplands (Table 2) were evaluated at P- and L-
348 band and H- and V-pol over the wheat-covered soil with different roughness structures using
349 the tau-omega model (Eq. 1), with the simulated and observed TB compared in Fig. 7. L-band
350 was found to substantially outperform P-band in all cases, indicating the inapplicability of the
351 default SMAP SCA parameters (Table 2) at P-band. Similar to Figs. 5 and 6, Fig. 7 also shows
352 a superior performance at V- over H-pol. More specifically, the RMSE at L-band was no higher
353 than 3 K at V-pol, demonstrating that the default SMAP SCA parameters were applicable to a
354 wide range of roughness and vegetation conditions with satisfactory accuracy. In the following,
355 only V-pol was analyzed due to its superiority over H-pol according to Figs. 6 and 7.

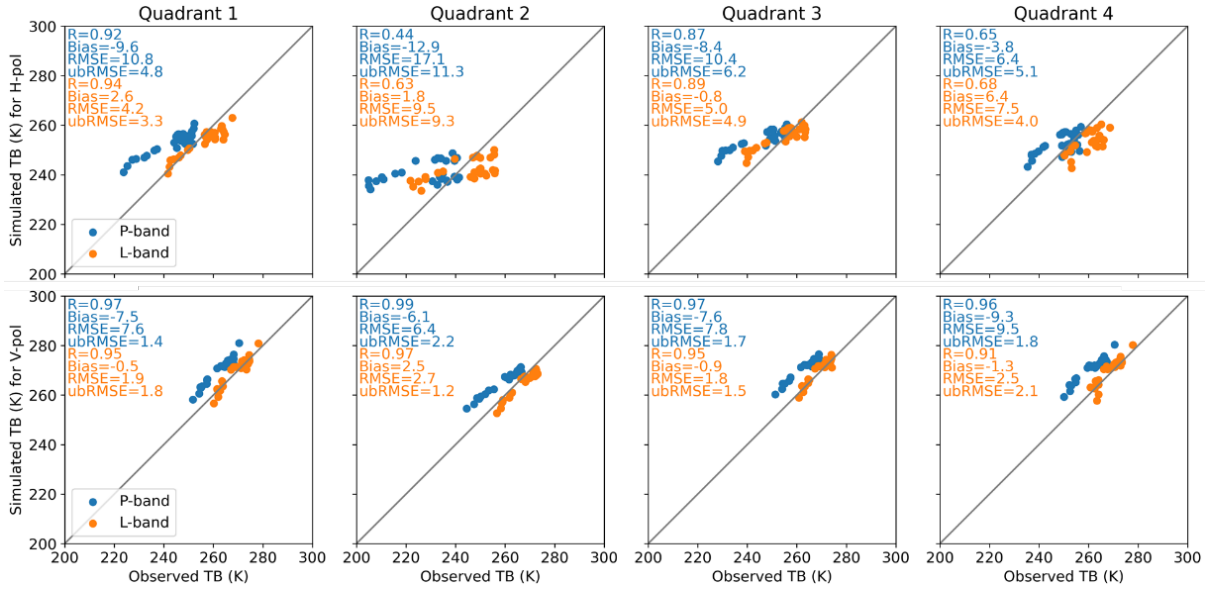


Fig. 7 Comparison of TB simulations against observations for H-pol (top row) and V-pol (bottom row) over the wheat-covered soil in each quadrant, using the SCA (Eq. 10) with the tau-omega model (Eq. 1). The default SMAP SCA parameters in Table 2 were used for all quadrants, both bands, and both polarizations.

356 The SMAP SCA parameters were demonstrated to work very well at L-band with low
 357 RMSE shown in Fig. 7, and therefore only the vegetation parameters (b and ω) at P-band were
 358 calibrated in Fig. 8. The soil moisture measurements collected over the wheat-covered soil
 359 were adopted to simulate TB, using the tau-omega model with calibrated H_R (Fig. 5) and
 360 varying b and ω . Overall, the b and ω values differed slightly across quadrants, ranging from
 361 0.099 to 0.150 and from 0.119 to 0.137, respectively (Fig. 8). The varied b and ω can be
 362 partially attributed to the different residuals of the roughness calibration (Fig. 5) that were left
 363 to be compensated by b and ω . Comparing the default and calibrated parameters, ω differed
 364 more considerably than other parameters, being 0.05 in the default configuration (Table 2) and
 365 ~ 0.12 - 0.13 after calibration (Fig. 8).

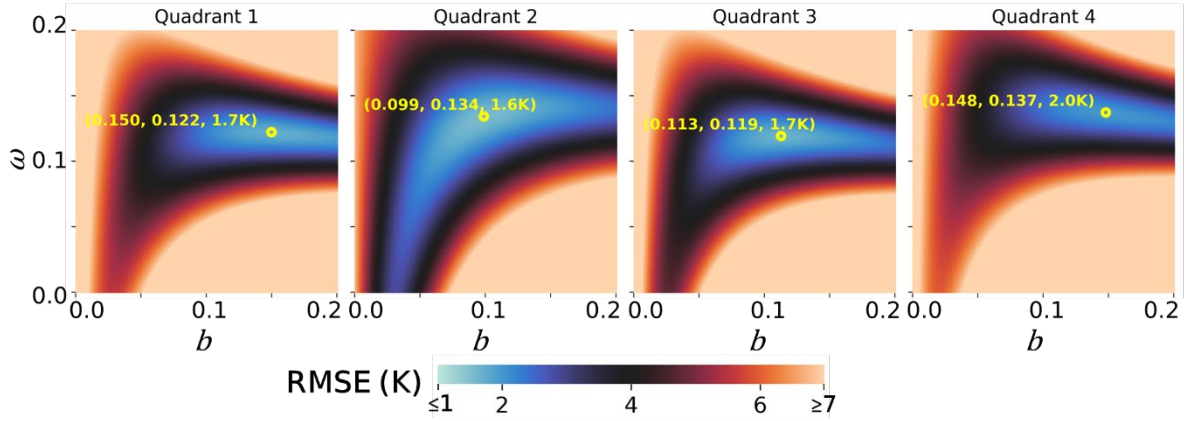


Fig. 8 RMSE (K) between the observed and simulated TB using a range of b and ω values for P-band V-pol over the wheat-covered soil in each quadrant. The tau-omega model (Eq. 1) was adopted as the forward model. The yellow circles indicate where the minimum RMSE was reached, with the three values showing b , ω , and the minimum RMSE, respectively. The calibrated H_R values at P-band V-pol from the period of bare soil, i.e., 0.174, 0.171, 0.070, and 0.092, were used for Q1-Q4, respectively. The parameters Q_R and N_{RP} were assumed to be the same as in the SMAP SCA, being 0 and 2, respectively.

366 The minimum RMSE was no higher than 2 K, indicating a good performance of the tau-
 367 omega model over the wheat-covered random and periodic soil. Additionally, even though the
 368 b and ω values denoted by the yellow circles in Fig. 8 are technically the calibrated parameters,
 369 a range of adjacent values can still be used if a certain calibration residual (e.g., 2 K) is tolerated.

370 Soil moisture was subsequently retrieved at P- and L-band V-pol using the tau-omega
371 model (Fig. 9). While the roughness (Fig. 5) and vegetation (Fig. 8) parameters were calibrated
372 at P-band in all four quadrants, only the parameters calibrated in Q2 ($H_R = 0.171$, $b = 0.099$,
373 and $\omega = 0.134$) were used for the soil moisture retrieval at P-band (Fig. 9). At L-band, the
374 SMAP SCA parameters (Table 2) were applied to the soil moisture retrieval (Fig. 9). It can be
375 seen from Fig. 9 that the RMSEs/ubRMSEs were similar across all four quadrants either at P-
376 or L-band (variations no more than $0.016 \text{ m}^3/\text{m}^3$), suggesting the possibility to ignore the
377 different roughness structures underneath vegetation when retrieving soil moisture.

378 5.3 DCA

379 Before applying the DCA soil moisture retrieval to the vegetated period, the full-time-
380 series TB and soil moisture during the bare soil period were used to calibrate the roughness

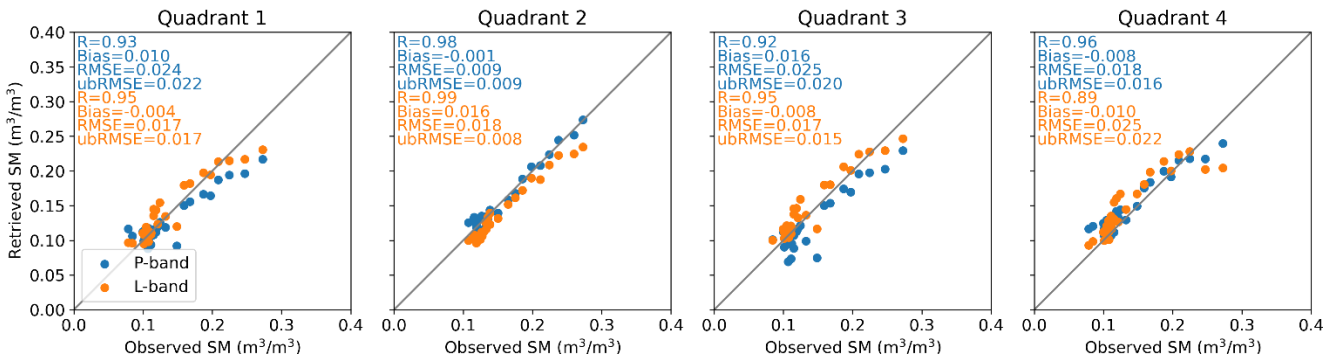


Fig. 9 Observed versus retrieved soil moisture over the wheat-covered soil in each quadrant, using the SCA-V (Eq. 10) with the tau-omega model (Eq. 1). The default SMAP SCA Q_R and N_{RP} and the calibrated H_R , b , and ω parameters in Q2 (flat soil) were used for P-band in all quadrants here, i.e., $Q_R = 0$, $N_{RP} = 2$, $H_R = 0.171$, $b = 0.099$, and $\omega = 0.134$. The default SMAP SCA parameters in Table 2 were used for L-band in all quadrants.

381 parameters, i.e., H_R and Q_R at P- and L-band in each quadrant, shown in Fig. 10. The H_R and
 382 Q_R values that produced the minimum RMSE were considered as the calibrated values, marked
 383 as the yellow circles with annotated values in Fig. 10.

384 Similar to Fig. 5, Fig. 10 also shows a lower RMSE at P- than L-band in the four quadrants,
 385 being 2.6-4.8 K and 5.4-10.8 K, respectively. This indicates that the HQN model performs
 386 better at P-band due to the reduced roughness impact. Q2 had the lowest calibration residual

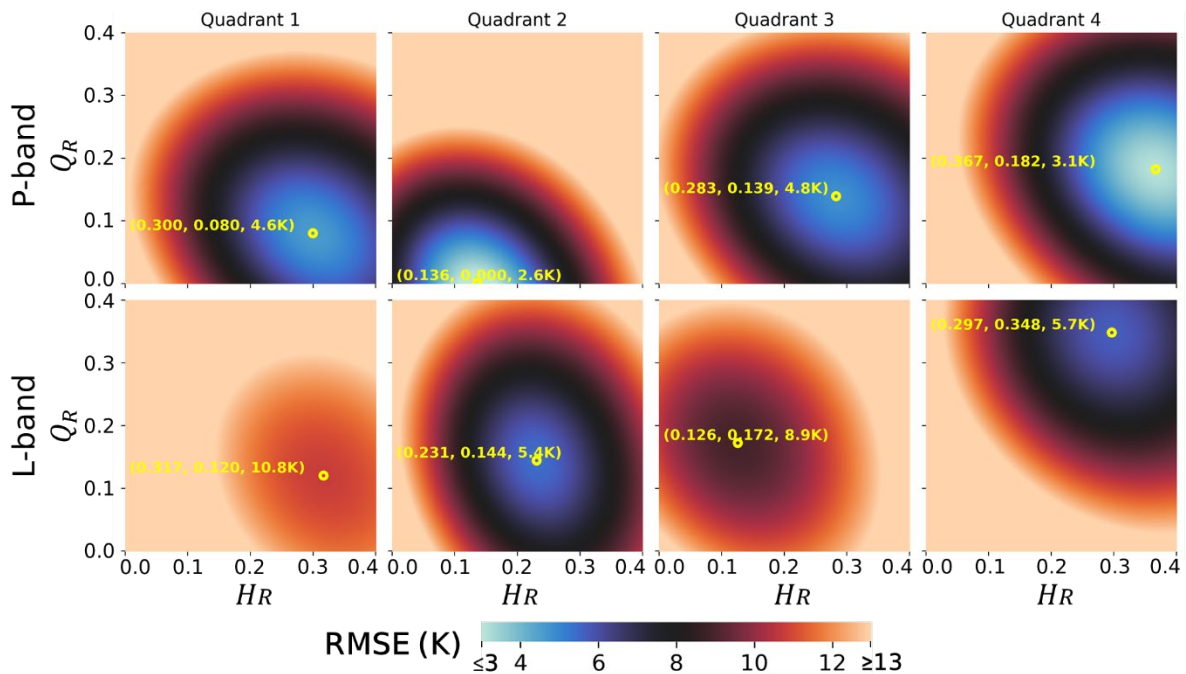


Fig. 10 RMSE (K) between the observed and simulated dual-pol TB using a range of H_R and Q_R values for P-band (top row) and L-band (bottom row) over the bare soil in each quadrant. The model for bare soil (Eq. 3) was adopted as the forward model. The yellow circles indicate where the minimum RMSE was reached, with the three values showing H_R , Q_R , and the minimum RMSE, respectively. The N_{RP} was assumed to be 2, the same as in the SMAP DCA, at both P- and L-band.

387 across the four quadrants for both P- and L-band because of its relatively smooth surface
388 compared to the periodic soil surfaces in Q1, Q3 and Q4. While Q_R is usually assumed to be
389 zero (e.g., Wigneron et al., 2001; Martens et al., 2015), this assumption was only found to be
390 valid at P-band but not at L-band in Q2 when using dual-pol TB, confirming the studies with
391 non-zero Q_R values at L-band (e.g., Lawrence et al., 2013). Moreover, Fig. 10 supports that
392 non-zero Q_R should apply for periodic surfaces when performing a DCA retrieval. It is also
393 worth noting that H_R and Q_R were larger in Q4 than Q3, particularly at L-band, indicating that
394 the periodic surface with parallel structures might have a larger impact than that with
395 perpendicular structures at $\sim 40^\circ$ incidence angle, in spite of the same row spacing and height.

396 Fig. 11 presents the comparison of the observed and retrieved soil moisture when applying
397 the H_R and Q_R calibrated in Q2 (Fig. 10) to all four quadrants. P-band was found to perform
398 better than L-band in all metrics. Similar to the SCA result in Fig. 9, the RMSEs and ubRMSEs
399 shown in Fig. 11 at either P- or L-band were comparable across the four quadrants, with
400 variations of no more than $0.011 \text{ m}^3/\text{m}^3$.

401 While the SMAP baseline algorithm has recently changed to the DCA from the SCA-V
402 due to the improved performance in some agricultural areas (O'Neill et al., 2021b), based on
403 Figs. 9 and 11 in this research, the DCA showed higher RMSE (e.g., $0.028 \text{ m}^3/\text{m}^3$ at P-band
404 and $0.062 \text{ m}^3/\text{m}^3$ at L-band in Q2) than the SCA-V (e.g., $0.009 \text{ m}^3/\text{m}^3$ at P-band and 0.018
405 m^3/m^3 at L-band in Q2). These results are consistent with the earlier validation results of SMAP
406 (Chan et al., 2016).

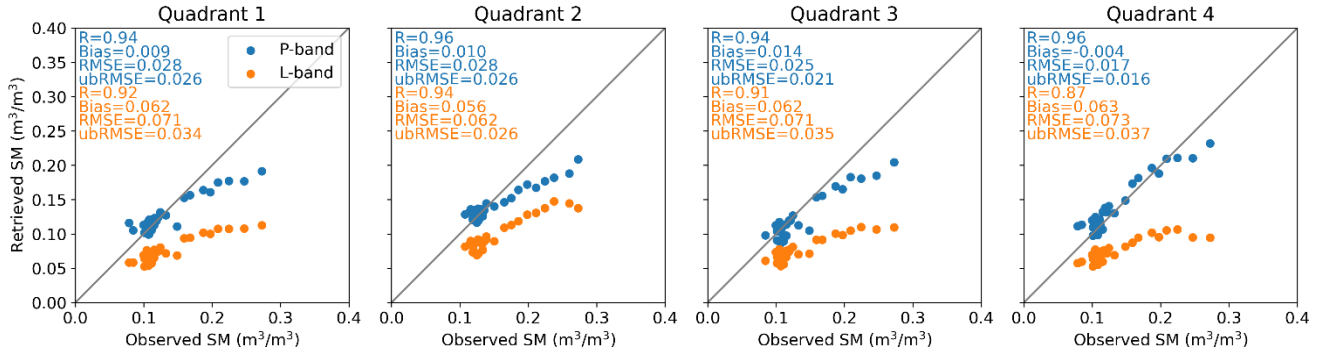


Fig. 11 Observed versus retrieved soil moisture over the wheat-covered soil in each quadrant, using the DCA (Eq. 11) with the tau-omega model (Eq. 1). The default SMAP DCA N_{RP} and ω were used for both P- and L-band, i.e., $N_{RP} = 2$ and $\omega = 0.06$. The calibrated H_R and Q_R from the period of bare flat soil in Q2 were used for all quadrants, i.e., $H_R = 0.136$ and $Q_R = 0$ for P-band and $H_R = 0.231$ and $Q_R = 0.144$ for L-band.

407 5.4 Estimation of vegetation impact

408 To investigate whether P-band had a reduced vegetation impact at P-band, the soil
 409 moisture was retrieved over the wheat-covered soil in Q2 without considering the vegetation
 410 impact in the model (Fig. 12), i.e., using the bare soil model (Eq. 3) with the calibrated H_R
 411 parameters in Fig. 5, being 0.171 for P-band and 0.081 for L-band. P-band was found to
 412 outperform L-band substantially in RMSE, being 0.029 and 0.063 m^3/m^3 for P- and L-band,
 413 respectively. The default SMAP H_R values for the SCA (0.15 for bare soil and 0.108 for
 414 croplands) were also investigated for both P- and L-band (not shown), and no discernable
 415 difference in RMSE was found compared to that in Fig. 12.

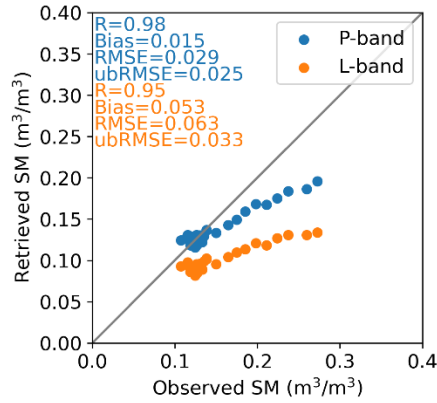


Fig. 12 Observed versus retrieved soil moisture over the wheat-covered soil in Q2, using the SCA-V (Eq. 10) with the bare soil forward model (Eq. 3). Calibrated H_R values from the period of bare flat soil in Q2 were used here, i.e., 0.171 for P-band and 0.081 for L-band, while Q_R and N_{RV} were assumed to be the same as those from the SMAP SCA at both P- and L-band, being 0 and 2, respectively.

416 6 Discussion

417 6.1 Do periodic surfaces need to be discriminated in soil moisture retrieval at P- and L- 418 band?

419 For the bare flat and periodic soil, the HQN model worked better at P- than L-band,
420 supported by the lower RMSE at P-band in the simulation results of Figs. 5 and 9. In terms of
421 soil moisture retrieval, P-band was also shown to have lower RMSE than L-band in Fig. 6.
422 Shen et al. (2022) pointed out that the default SMAP and SMOS parameters induced larger
423 errors over periodic surfaces than flat surfaces. In the current investigation, the H_R was
424 calibrated in Q2 and then applied to retrieve the soil moisture in all four quadrants, with the
425 result showing that P-band had a reduced error compared to L-band (Fig. 6). This evidence

426 collectively confirms the conclusion by Shen et al. (2022) that P-band was less impacted by
427 random and periodic roughness than L-band.

428 For the wheat-covered soil with different roughness structures, the default SMAP SCA
429 parameters were found to work very well at L-band but not at P-band (Fig. 7). Moreover, the
430 calibrated parameters at P-band led to an RMSE similar to that obtained at L-band using the
431 default SMAP SCA parameters, being no higher than 3 K (Figs. 7 and 8). From the aspect of
432 soil moisture retrieval, no substantial variation across different quadrants was observed at both
433 P- and L-band whether using the SCA (Fig. 9) or the DCA (Fig. 11), indicating that the same
434 parameters can be used for wheat-covered soil with different roughness structures.

435 In summary, P-band did not need to have the periodic surfaces discriminated for either
436 bare or wheat-covered soil, while L-band needed differently calibrated parameters for bare
437 periodic surfaces compared to bare flat surfaces due to the more considerable roughness impact.
438 However, when the wheat canopy covered the soil, the periodicity of the surfaces no longer
439 needed to be considered at L-band. A possible explanation is that the mature wheat canopy
440 “masked” the roughness structures below.

441 **6.2 Can low-to-intermediate vegetation be omitted in soil moisture retrieval at P- and L-** 442 **band?**

443 When using one TB observation to retrieve one soil moisture using the tau-omega model
444 (i.e., the SCA), prior vegetation information (e.g., VWC, NDVI (Normalized Difference
445 Vegetation Index), LAI (Leaf Area Index, Yadav et al., 2020), etc.) is required to estimate τ

446 using Eq. 9. When such information is not available, the use of P-band observations can still
447 achieve an acceptable performance ($0.029 \text{ m}^3/\text{m}^3$ in RMSE) when completely ignoring the
448 vegetation impact by using the bare soil model (Fig. 12). In contrast, the corresponding RMSE
449 at L-band was as high as $0.063 \text{ m}^3/\text{m}^3$, demonstrating that the impact of low-to-intermediate
450 vegetation (under $4 \text{ kg}/\text{m}^2$) can be neglected at P-band but not at L-band.

451 Neglecting the vegetation resulted in underestimating the soil moisture observations (Fig.
452 12) because the vegetation contribution was mistakenly considered as a soil contribution,
453 increasing the soil emissivity and thus decreasing the soil moisture. This phenomenon was
454 particularly prominent for high soil moisture (Fig. 12) when the VWC was also high (Fig. 4).
455 Consequently, it can be postulated that the advantage of P- over L-band in reducing the
456 vegetation impact will become more considerable when the VWC achieves a higher range, e.g.,
457 corn (Hornbuckle and England, 2004).

458 **6.3 Are model parameters comparable across different frequencies?**

459 Directly comparing the model parameters (i.e., H_R , Q_R , b , and ω) across different
460 frequencies seems to be a straightforward way to judge the reduced roughness and vegetation
461 impact at a specific frequency compared to others. However, this might not actually make sense.
462 Gao et al. (2017) calibrated the H_R and b at L-, C- and X-band by assuming $\omega = 0.05$ and found
463 H_R and b increased with increasing frequency. On the contrary, Wang et al. (1983) discovered
464 that H_R did not have a definitive relation to frequency. While Mo et al. (1982) obtained higher
465 H_R and b values at C-band than those at L-band, consistent with Gao et al. (2017), they found

466 ω was higher at L-band, contradictory to microwave radiometry theory which suggests that a
467 longer wavelength band should have reduced scattering effects. Additionally, considering the
468 results in this paper (Figs. 5, 8, and 10) where no explicit frequency-dependence was found for
469 the parameters H_R , b , and ω , it might be concluded that these model parameters should not be
470 compared across different frequencies.

471 Two reasons can be attributed to the incomparability of those model parameters. First, the
472 tau-omega and the HQN models are semi-empirical, approximating the rigorous physical
473 process by linking the model parameters (i.e., H_R , b , and ω) to some measurable variables (e.g.,
474 rms height, correlation length, and VWC). Meanwhile, many assumptions have been made to
475 develop simplified analytical equations, including the homogeneity of soil moisture in space
476 and with depth, the scattering isotropy of soil and vegetation, and the negligibility of the high-
477 order scattering. Therefore, these parameters have to be considered as effective rather than
478 physical (Wigneron et al., 2017).

479 Second, the mismatch between the sampling depth of the soil moisture measurements and
480 the theoretical moisture retrieval depth may also lead to an incomparability of model
481 parameters. The moisture retrieval depth is dependent on frequency and moisture profile and
482 is thus a time-variant variable (Shen et al., 2021), making it impractical to calibrate the model
483 parameters using the soil moisture observations exactly within the moisture retrieval depth, let
484 alone the challenge to measure the continuous soil moisture in a very thin layer, e.g., 1-2 cm.

485 The Q_R was found to be a possible exception from both the literature and current results
486 when estimated to be non-zero. Fig. 10 presents that the Q_R values at P-band were lower than

487 those at L-band in all four quadrants. Similarly, Wang et al. (1983) has reported that while H_R
488 is not correlated to frequency, such a relation exists for Q_R , being 0.01, 0.15, and 0.20 at 1.4,
489 5, and 10.7 GHz, respectively, for a soil surface with 0.73-cm rms height. However, such a
490 conclusion is drawn with much caution, given that relevant studies mostly assumed constant
491 Q_R (e.g., Wigneron et al., 2001; Martens et al., 2015) and thus more evidence is still required.

492 **6.4 What are the challenges of a successful P-band-radiometer mission?**

493 While it has been demonstrated that P-band is a promising proposition to replace or
494 enhance the current L-band SMOS and SMAP missions in the forthcoming years, so as to
495 obtain deeper and more accurate soil moisture information (Shen et al., 2021; Shen et al., 2022),
496 there remain four challenges: aperture size, radio frequency interference (RFI), receiver design
497 and calibration, and ionospheric and celestial emission effects (Johnson et al., 2021).

498 With the spatial resolution of a radiometer determined by the size of the antenna relative
499 to the observing wavelength for a given orbit altitude, the aperture of a 0.75-GHz radiometer
500 needs to be enlarged by 1.87 times to retain the same 40-km spatial resolution of the 1.4-GHz
501 radiometer of SMAP, i.e., increasing from the 6-m-diameter antenna of SMAP to an 11.22-m-
502 diameter antenna. Moreover, unlike L-band (1.400-1.427 GHz) that is exclusively allocated for
503 radio astronomy use, P-band (0.3-1 GHz) is heavily occupied by television broadcast,
504 communications, and other applications (National Research Council, 2010), easily causing RFI
505 and corrupting radiometric measurements from the target. Additionally, at 0.75 GHz, the

506 amount of Faraday rotation and ionosphere-specific attenuation is approximately 3.5 times as
507 large as at 1.4 GHz, which needs to be corrected.

508 Nowadays, large deployable antennas (e.g., Meguro et al., 2009) and highly developed
509 downscaling techniques (Peng et al., 2017; Sabaghy et al., 2018; Sharma et al., 2021) make
510 higher spatial resolution at P-band possible. Moreover, RFI mitigation techniques are
511 becoming increasingly mature (Skou et al., 2009; Huang et al., 2018; Jin et al., 2019). The
512 ultra-wideband software defined microwave radiometer (UWBRAD) is a successful example
513 in this regard for demonstrating how a future P-band-radiometer mission might address the RFI
514 issue (Johnson et al., 2016; Yardim et al., 2021). The UWBRAD detects and filters RFI by
515 segmenting the observed bandwidth (from 0.5 to 2 GHz) into 12 channels, each of which is
516 further resolved into 512 subchannels, so that the RFI-free portions of the spectrum can be
517 identified and integrated. These advancements in aerospace and remote sensing technologies
518 pave the way for a successful P-band-radiometer mission in the near future.

519 **7 Conclusion**

520 This paper evaluated the tau-omega model over bare and wheat-covered flat and periodic
521 surfaces at P- and L-band to demonstrate the potential improvement in soil moisture retrieval
522 from using the longer wavelength P-band observations. For the bare flat and periodic soil
523 surfaces, V-pol was less impacted by roughness impact than H-pol at both P- and L-band in
524 terms of both TB simulation and soil moisture retrieval. Evaluating the SCA-V retrieval results
525 showed that P-band had a more comparable RMSE than those at L-band across different

526 roughness configurations, with variations being up to 0.012 and 0.022 m³/m³ for P- and L-band,
527 respectively.

528 For the wheat-covered soil, the default SMAP SCA parameters for croplands were found
529 to simulate TB satisfactorily at L-band V-pol but not at L-band H-pol or P-band. Therefore, at
530 P-band V-pol, the roughness and vegetation parameters were calibrated in Q2 (flat soil) and
531 applied to retrieve the soil moisture in all four quadrants, while the default SMAP parameters
532 were applied to retrieve the soil moisture in all four quadrants at L-band V-pol. The RMSE
533 between observed and retrieved soil moisture showed that neither P- or L-band had substantial
534 performance variation across different quadrants for the SCA or DCA. However, the DCA had
535 a degraded retrieval performance compared to the SCA-V.

536 In short, P-band had a reduced roughness impact and was thus able to model both the flat
537 and periodic soil using the calibrated parameters from the flat soil, for both bare and wheat-
538 covered soil. Conversely, L-band could only treat the different periodic surfaces like a flat
539 surface when covered by a mature wheat canopy. Moreover, a lower RMSE at P-band (0.029
540 m³/m³) than L-band (0.063 m³/m³) was observed when omitting vegetation effects in the
541 forward model, confirming that P-band observations were relatively unaffected by the wheat
542 canopy.

543 **Acknowledgment**

544 This work was supported by the Australian Research Council through the Towards P-
545 Band Soil Moisture Sensing from Space Project under Discovery Grant DP170102373, and

546 Linkage, Infrastructure, Equipment and Facility Grants LE0453434 and LE150100047. This
547 work was also supported in part by the China Scholarship Council. The authors wish to thank
548 Pascal Mater and Kiri Mason for their help with the experimental equipment and site
549 maintenance. Thanks also to Mr. Wayne Tymensen for kindly providing the land for the
550 experiment site.

551 **References**

- 552 Alemohammad, S.H., Jagdhuber, T., Moghaddam, M., & Entekhabi, D. (2019). Soil and
553 vegetation scattering contributions in L-band and P-band polarimetric SAR observations. *IEEE*
554 *Transactions on Geoscience and Remote Sensing*
- 555 Basharinov, A.Y., & Shutko, A. (1975). Simulation studies of the SHF radiation characteristics
556 of soils under moist conditions.
- 557 Chan, S.K., Bindlish, R., O'Neill, P.E., Njoku, E., Jackson, T., Colliander, A., Chen, F., Burgin,
558 M., Dunbar, S., & Piepmeier, J. (2016). Assessment of the SMAP Passive Soil Moisture
559 Product. *IEEE Transactions on Geoscience and Remote Sensing*, *54*, 4994-5007
- 560 Choudhury, B.J., Schmugge, T.J., Chang, A., & Newton, R.W. (1979). Effect of surface
561 roughness on the microwave emission from soils. *Journal of Geophysical Research: Oceans*,
562 *84*, 5699-5706
- 563 Choudhury, B.J., Schmugge, T.J., & Mo, T. (1982). A parameterization of effective soil
564 temperature for microwave emission. *Journal of Geophysical Research: Oceans*, *87*, 1301–
565 1304
- 566 Colliander, A., Jackson, T.J., Bindlish, R., Chan, S., Das, N., Kim, S., Cosh, M., Dunbar, R.,
567 Dang, L., & Pashaian, L. (2017). Validation of SMAP surface soil moisture products with core
568 validation sites. *Remote Sensing of Environment*, *191*, 215-231
- 569 Council, N.R. (2010). *Spectrum management for science in the 21st century*. National
570 Academies Press
- 571 Crow, W.T., Milak, S., Moghaddam, M., Tabatabaenejad, A., Jaruwatanadilok, S., Yu, X., Shi,
572 Y., Reichle, R.H., Hagimoto, Y., & Cuenca, R.H. (2018). Spatial and temporal variability of
573 root-zone soil moisture acquired from hydrologic modeling and AirMOSS P-band radar. *IEEE*
574 *Journal of Selected Topics in Applied Earth Observations and Remote Sensing*, *11*, 4578-4590

- 575 Entekhabi, D., Njoku, E.G., O'Neill, P.E., Kellogg, K.H., Crow, W.T., Edelstein, W.N., Entin,
576 J.K., Goodman, S.D., Jackson, T.J., Johnson, J., Kimball, J., Piepmeier, J.R., Koster, R.D.,
577 Martin, N., McDonald, K.C., Moghaddam, M., Moran, S., Reichle, R., Shi, J.C., Spencer, M.W.,
578 Thurman, S.W., Tsang, L., & Van Zyl, J. (2010). The Soil Moisture Active Passive (SMAP)
579 Mission. *Proceedings of the IEEE*, 98, 704-716
- 580 Entekhabi, D., Yueh, S., O'Neill, P.E., Kellogg, K.H., Allen, A., Bindlish, R., Brown, M., Chan,
581 S., Colliander, A., & Crow, W.T. (2014). SMAP handbook—Soil Moisture Active Passive:
582 Mapping soil moisture and freeze/thaw from space
- 583 Escorihuela, M.J., Chanzy, A., Wigneron, J.P., & Kerr, Y.H. (2010). Effective soil moisture
584 sampling depth of L-band radiometry: A case study. *Remote Sensing of Environment*, 114, 995-
585 1001
- 586 Fagerlund, E., Kleman, B., Sellin, L., & Svensson, H. (1970). Physical studies of nature by
587 thermal mapping. *Earth-Science Reviews*, 6, 169-180
- 588 Gao, Y., Colliander, A., Burgin, M.S., Walker, J.P., Chae, C., Dinnat, E., & Cosh, M.H. (2017).
589 Multi-frequency radiometer-based soil moisture retrieval algorithm parametrization using in
590 situ validation sites. In, *2017 IEEE International Geoscience and Remote Sensing Symposium*
591 *(IGARSS)* (pp. 3945-3948): IEEE
- 592 Gao, Y., Walker, J.P., Ye, N., Panciera, R., Monerris, A., Ryu, D., Rüdiger, C., & Jackson, T.J.
593 (2018). Evaluation of the tau-omega model for passive microwave soil moisture retrieval using
594 SMAPEX datasets. *IEEE Journal of Selected Topics in Applied Earth Observations and Remote*
595 *Sensing*, 11, 888-895
- 596 Garrison, J., Shah, R., Nold, B., Mansell, J., Vega, M., Raymond, J., Bindlish, R., Kurum, M.,
597 Piepmeier, J., & Kim, S. (2021). SNOOPI: Demonstrating P-band reflectometry from orbit. In,
598 *2021 IEEE International Geoscience and Remote Sensing Symposium (IGARSS)* (pp. 164-167):
599 IEEE
- 600 Hornbuckle, B., & England, A. (2004). Radiometric sensitivity to soil moisture at 1.4 GHz
601 through a corn crop at maximum biomass. *Water Resources Research*, 40
- 602 Huang, Y., Liao, G., Li, J., & Xu, J. (2018). Narrowband RFI suppression for SAR system via
603 fast implementation of joint sparsity and low-rank property. *IEEE Transactions on Geoscience*
604 *and Remote Sensing*, 56, 2748-2761
- 605 ITU (2015). International Telecommunication Union recommendation: Radio noise. In: ITU-
606 R P.372-12
- 607 Jackson, T.J. (1993). III. Measuring surface soil moisture using passive microwave remote
608 sensing. *Hydrological Processes*, 7, 139–152

- 609 Jackson, T.J., & Schmugge, T.J. (1991). Vegetation effects on the microwave emission of soils.
610 *Remote Sensing of Environment*, 36, 203-212
- 611 Jackson, T.J., Schmugge, T.J., & Wang, J.R. (1982). Passive microwave sensing of soil
612 moisture under vegetation canopies. *Water Resources Research*, 18, 1137-1142
- 613 Jin, R., Li, Q., & Liu, H. (2019). A subspace algorithm to mitigate energy unknown RFI for
614 synthetic aperture interferometric radiometer. *IEEE Transactions on Geoscience and Remote
615 Sensing*, 58, 227-237
- 616 Johnson, J.T., Jezek, K.C., Aksoy, M., Bringer, A., Yardim, C., Andrews, M., Chen, C.-C.,
617 Belgiovane, D., Leuski, V., & Durand, M. (2016). The Ultra-wideband Software-Defined
618 Radiometer (UWBRAD) for ice sheet internal temperature sensing: Results from recent
619 observations. In, *2016 IEEE International Geoscience and Remote Sensing Symposium
620 (IGARSS)* (pp. 7085-7087): IEEE
- 621 Johnson, J.T., Jezek, K.C., Macelloni, G., Brogioni, M., Tsang, L., Dinnat, E.P., Walker, J.P.,
622 Ye, N., Misra, S., & Piepmeier, J.R. (2021). Microwave radiometry at frequencies from 500 to
623 1400 MHz: An emerging technology for earth observations. *IEEE Journal of Selected Topics
624 in Applied Earth Observations and Remote Sensing*, 14, 4894-4914
- 625 Kerr, Y.H., Waldteufel, P., Richaume, P., Ferrazzoli, P., & Wigneron, J.P. (2019). Algorithm
626 theoretical basis document (ATBD) for the SMOS level 2 soil moisture processor development
627 continuation project v4.0. In (p. 150).
628 <https://earth.esa.int/eogateway/documents/20142/37627/SMOS-L2-SM-ATBD.pdf>: SM-ESL
629 (CBSA)
- 630 Kerr, Y.H., Waldteufel, P., Wigneron, J.-P., Delwart, S., Cabot, F., Boutin, J., Escorihuela, M.-
631 J., Font, J., Reul, N., Gruhier, C., Juglea, S.E., Drinkwater, M.R., Hahne, A., Martin-Neira, M.,
632 & Mecklenburg, S. (2010). The SMOS mission: New tool for monitoring key elements of the
633 global water cycle. *Proceedings of the IEEE*, 98, 666-687
- 634 Konings, A.G., Piles, M., Das, N., & Entekhabi, D. (2017). L-band vegetation optical depth
635 and effective scattering albedo estimation from SMAP. *Remote Sensing of Environment*, 198,
636 460-470
- 637 Konings, A.G., Piles, M., Rötzer, K., Mccoll, K.A., Chan, S.K., & Entekhabi, D. (2016).
638 Vegetation optical depth and scattering albedo retrieval using time series of dual-polarized L-
639 band radiometer observations. *Remote Sensing of Environment*, 172, 178-189
- 640 Koster, R.D., Dirmeyer, P.A., Guo, Z., Bonan, G., Chan, E., Cox, P., Gordon, C., Kanae, S.,
641 Kowalczyk, E., & Lawrence, D. (2004). Regions of strong coupling between soil moisture and
642 precipitation. *Science*, 305, 1138-1140
- 643 Kraft, D. (1988). A software package for sequential quadratic programming

- 644 Lawrence, H., Wigneron, J.P., Demontoux, F., Mialon, A., & Kerr, Y.H. (2013). Evaluating the
645 semiempirical H–Q model used to calculate the L-band emissivity of a rough bare soil. *IEEE*
646 *Transactions on Geoscience and Remote Sensing*, *51*, 4075-4084
- 647 Le Toan, T., Quegan, S., Davidson, M., Balzter, H., Paillou, P., Papathanassiou, K., Plummer,
648 S., Rocca, F., Saatchi, S., & Shugart, H. (2011). The BIOMASS mission: Mapping global forest
649 biomass to better understand the terrestrial carbon cycle. *Remote Sensing of Environment*, *115*,
650 2850-2860
- 651 Li, X., Al-Yaari, A., Schwank, M., Fan, L., Frappart, F., Swenson, J., & Wigneron, J.-P. (2020).
652 Compared performances of SMOS-IC soil moisture and vegetation optical depth retrievals
653 based on Tau-Omega and Two-Stream microwave emission models. *Remote Sensing of*
654 *Environment*, *236*, 111502
- 655 Liu, P.-W., De Roo, R.D., England, A.W., & Judge, J. (2012). Impact of moisture distribution
656 within the sensing depth on L-and C-band emission in sandy soils. *IEEE Journal of Selected*
657 *Topics in Applied Earth Observations and Remote Sensing*, *6*, 887-899
- 658 Martens, B., Lievens, H., Colliander, A., Jackson, T.J., & Verhoest, N.E.C. (2015). Estimating
659 effective roughness parameters of the L-MEB model for soil moisture retrieval using passive
660 microwave observations from SMAPVEX12. *IEEE Transactions on Geoscience and Remote*
661 *Sensing*, *53*, 4091-4103
- 662 Meguro, A., Shintate, K., Usui, M., & Tsujihata, A. (2009). In-orbit deployment characteristics
663 of large deployable antenna reflector onboard Engineering Test Satellite VIII. *Acta*
664 *Astronautica*, *65*, 1306-1316
- 665 Merlin, O., Walker, J.P., Panciera, R., Young, R., Kalma, J.D., & Kim, E.J. (2007). Soil
666 moisture measurement in heterogeneous terrain. In, *Modsim International Congress on*
667 *Modelling & Simulation Land Water & Environmental Management Integrated Systems for*
668 *Sustainability* (pp. 2604-2610)
- 669 Mironov, V., Kerr, Y., Wigneron, J.P., Kosolapova, L., & Demontoux, F. (2013a). Temperature-
670 and texture-dependent dielectric model for moist soils at 1.4 GHz. *IEEE Geoscience and*
671 *Remote Sensing Letters*, *10*, 419-423
- 672 Mironov, V.L., Bobrov, P.P., & Fomin, S.V. (2013b). Multirelaxation generalized refractive
673 mixing dielectric model of moist soils. *IEEE Geoscience and Remote Sensing Letters*, *10*, 603-
674 606
- 675 Mo, T., Choudhury, B.J., Schmugge, T.J., Wang, J.R., & Jackson, T.J. (1982). A model for
676 microwave emission from vegetation-covered fields. *Journal of Geophysical Research:*
677 *Oceans*, *87*, 11229-11237
- 678 Newton, R.W., & Rouse, J.W. (1980). Microwave radiometer measurements of soil moisture

679 content. *IEEE Transactions on Antennas and Propagation*, 28, 680 - 686

680 Njoku, E.G., & Chan, S.K. (2006). Vegetation and surface roughness effects on AMSR-E land
681 observations. *Remote Sensing of Environment*, 100, 190-199

682 Njoku, E.G., Jackson, T.J., Lakshmi, V., Chan, T.K., & Nghiem, S.V. (2003). Soil moisture
683 retrieval from AMSR-E. *IEEE Transactions on Geoscience and Remote Sensing*, 41, 215-229

684 Njoku, E.G., & Li, L. (1999). Retrieval of land surface parameters using passive microwave
685 measurements at 6-18 GHz. *IEEE Transactions on Geoscience and Remote Sensing*, 37, 79-93

686 O'Neill, P., Bindlish, R., Chan, S., Chaubell, J., Colliander, A., Njoku, E., & Jackson, T. (2021a).
687 SMAP algorithm theoretical basis document (ATBD) level 2 & 3 soil moisture (passive) data
688 products revision G. In (p. 111). <https://nsidc.org/data/smap/technical-references>: Jet
689 Propulsion Laboratory

690 O'Neill, P., Chan, S., Bindlish, R., Chaubell, M., Colliander, A., Chen, F., Dunbar, S., Jackson,
691 T., Peng, J., Mousavi, M., Cosh, M., Bongiovanni, T., Walker, J., Wu, X., Berg, A., McNairn,
692 H., Thibeault, M., Martínez-Fernández, J., González-Zamora, Á., Lopez-Baeza, E., Jensen, K.,
693 Seyfried, M., Bosch, D., Starks, P., Collins, C.H., Prueger, J., Su, Z., Velde, R.v.d., Asanuma,
694 J., Palecki, M., Small, E., Zreda, M., Calvet, J., Crow, W., Kerr, Y., Yueh, S., & Entekhabi, D.
695 (2021b). Calibration and validation for the L2/3_SM_P version 8 and L2/3_SM_P_E version
696 5 data products. In (p. 67). <https://nsidc.org/data/smap/technical-references>: Jet Propulsion
697 Laboratory

698 Oki, T., & Kanae, S. (2006). Global hydrological cycles and world water resources. *Science*,
699 313, 1068

700 Owe, M., de Jeu, R.A.M., & Walker, J. (2001). A methodology for surface soil moisture and
701 vegetation optical depth retrieval using the microwave polarization difference index. *IEEE*
702 *Transactions on Geoscience and Remote Sensing*, 39, 1643-1654

703 Patton, J., & Hornbuckle, B. (2012). Initial validation of SMOS vegetation optical thickness in
704 Iowa. *IEEE Geoscience and Remote Sensing Letters*, 10, 647-651

705 Peng, J., Loew, A., Merlin, O., & Verhoest, N.E. (2017). A review of spatial downscaling of
706 satellite remotely sensed soil moisture. *Reviews of Geophysics*, 55, 341-366

707 Prigent, C., Wigneron, J.-P., Rossow, W.B., & Pardo-Carrion, J.R. (2000). Frequency and
708 angular variations of land surface microwave emissivities: Can we estimate SSM/T and AMSU
709 emissivities from SSM/I emissivities? *IEEE Transactions on Geoscience and Remote Sensing*,
710 38, 2373-2386

711 Sabaghy, S., Walker, J.P., Renzullo, L.J., & Jackson, T.J. (2018). Spatially enhanced passive
712 microwave derived soil moisture: Capabilities and opportunities. *Remote Sensing of*

- 713 *Environment*, 209, 551-580
- 714 Seneviratne, S.I., Corti, T., Davin, E.L., Hirschi, M., Jaeger, E.B., Lehner, I., Orlowsky, B., &
715 Teuling, A.J. (2010). Investigating soil moisture–climate interactions in a changing climate: A
716 review. *Earth-Science Reviews*, 99, 125-161
- 717 Sharma, J., Prasad, R., Srivastava, P.K., Singh, S.K., Yadav, S.A., & Yadav, V.P. (2021).
718 Roughness characterization and disaggregation of coarse resolution SMAP soil moisture using
719 single-channel algorithm. *Journal of Applied Remote Sensing*, 15, 014514
- 720 Shen, X., Walker, J.P., Ye, N., Wu, X., Boopathi, N., Yeo, I.-Y., Zhang, L., & Zhu, L. (2021).
721 Soil moisture retrieval depth of P- and L-band radiometry: predictions and observations. *IEEE*
722 *Transactions on Geoscience and Remote Sensing*, 59, 6814-6822
- 723 Shen, X., Walker, J.P., Ye, N., Wu, X., Brakhasi, F., Boopathi, N., Zhu, L., Yeo, I.-Y., Kim, E.,
724 Kerr, Y., & Jackson, T. (2022). Impact of random and periodic surface roughness on P- and L-
725 band radiometry. *Remote Sensing of Environment*, 269, 112825
- 726 Shiklomanov, I.A. (1993). World fresh water resources. In P.H. Gleick (Ed.), *Water in Crisis:*
727 *A Guide to the World's Fresh Water Resources*. New York: Oxford University Press
- 728 Skou, N., Misra, S., Balling, J.E., Kristensen, S.S., & Sobjaerg, S.S. (2009). L-band RFI as
729 experienced during airborne campaigns in preparation for SMOS. *IEEE Transactions on*
730 *Geoscience and Remote Sensing*, 48, 1398-1407
- 731 Tabatabaenejad, A., Burgin, M., Duan, X., & Moghaddam, M. (2014). P-band radar retrieval
732 of subsurface soil moisture profile as a second-order polynomial: First AirMOSS results. *IEEE*
733 *Transactions on Geoscience and Remote Sensing*, 53, 645-658
- 734 Tabatabaenejad, A., Chen, R.H., Burgin, M.S., Duan, X., Cuenca, R.H., Cosh, M.H., Scott,
735 R.L., & Moghaddam, M. (2020). Assessment and validation of AirMOSS P-band root-zone
736 soil moisture products. *IEEE Transactions on Geoscience and Remote Sensing*, 58, 6181-6196
- 737 Ulaby, F.T., Long, D.G., Blackwell, W.J., Elachi, C., Fung, A.K., Ruf, C., Sarabandi, K., Zebker,
738 H.A., & Van Zyl, J. (2014). *Microwave radar and radiometric remote sensing*. University of
739 Michigan Press Ann Arbor
- 740 Ulaby, F.T., Moore, R.K., & Fung, A.K. (1982). *Microwave remote sensing active and passive-*
741 *Volume II: Radar remote sensing and surface scattering and emission theory*. Artech House Inc.
- 742 Ulaby, F.T., Moore, R.K., & Fung, A.K. (1986). *Microwave remote sensing active and passive-*
743 *Volume III: From theory to applications*. Artech House Inc.
- 744 Wagner, N., Emmerich, K., Bonitz, F., & Kupfer, K. (2011). Experimental investigations on
745 the frequency- and temperature-dependent dielectric material properties of soil. *IEEE*
746 *Transactions on Geoscience and Remote Sensing*, 49, 2518-2530

- 747 Walker, V.A., Hornbuckle, B.K., Cosh, M.H., & Prueger, J.H. (2019). Seasonal evaluation of
748 SMAP soil moisture in the US corn belt. *Remote Sensing*, *11*, 2488
- 749 Wang, J.R., & Choudhury, B.J. (1981). Remote sensing of soil moisture content, over bare field
750 at 1.4 GHz frequency. *Journal of Geophysical Research: Oceans*, *86*, 5277-5282
- 751 Wang, J.R., O'Neill, P.E., Jackson, T.J., & Engman, E.T. (1983). Multifrequency measurements
752 of the effects of soil moisture, soil texture, and surface roughness. *IEEE Transactions on*
753 *Geoscience and Remote Sensing*, *21:1*, 44-51
- 754 Wigneron, J.-P., Chanzy, A., Calvet, J.-C., & Bruguier, N. (1995). A simple algorithm to
755 retrieve soil moisture and vegetation biomass using passive microwave measurements over
756 crop fields. *Remote Sensing of Environment*, *51*
- 757 Wigneron, J.P., Jackson, T.J., O'Neill, P., De Lannoy, G., de Rosnay, P., Walker, J.P., Ferrazzoli,
758 P., Mironov, V., Bircher, S., Grant, J.P., Kurum, M., Schwank, M., Munoz-Sabater, J., Das, N.,
759 Royer, A., Al-Yaari, A., Al Bitar, A., Fernandez-Moran, R., Lawrence, H., Mialon, A., Parrens,
760 M., Richaume, P., Delwart, S., & Kerr, Y. (2017). Modelling the passive microwave signature
761 from land surfaces: A review of recent results and application to the L-band SMOS & SMAP
762 soil moisture retrieval algorithms. *Remote Sensing of Environment*, *192*, 238-262
- 763 Wigneron, J.P., Kerr, Y., Waldteufel, P., Saleh, K., Escorihuela, M.J., Richaume, P., Ferrazzoli,
764 P., Rosnay, P.D., Gurney, R., & Calvet, J.C. (2007). L-band Microwave Emission of the
765 Biosphere (L-MEB) Model: Description and calibration against experimental data sets over
766 crop fields. *Remote Sensing of Environment*, *107*, 639-655
- 767 Wigneron, J.P., Laguerre, L., & Kerr, Y.H. (2001). A simple parameterization of the L-band
768 microwave emission from rough agricultural soils. *IEEE Transactions on Geoscience and*
769 *Remote Sensing*, *39*, 1697-1707
- 770 Yadav, V.P., Prasad, R., Bala, R., & Srivastava, P.K. (2020). Synergy of Vegetation and Soil
771 Microwave Scattering Model for Leaf Area Index Retrieval Using C-Band Sentinel-1A
772 Satellite Data. *IEEE Geoscience and Remote Sensing Letters*
- 773 Yardim, C., Johnson, J.T., Jezek, K.C., Andrews, M.J., Durand, M., Duan, Y., Tan, S., Tsang,
774 L., Brogioni, M., & Macelloni, G. (2021). Greenland ice sheet subsurface temperature
775 estimation using ultrawideband microwave radiometry. *IEEE Transactions on Geoscience and*
776 *Remote Sensing*
- 777 Yueh, S., Shah, R., Xu, X., Elder, K., & Starr, B. (2020). Experimental demonstration of soil
778 moisture remote sensing using P-band satellite signals of opportunity. *IEEE Geoscience and*
779 *Remote Sensing Letters*, *17*, 207-211
- 780 Zhao, T., Hu, L., Shi, J., Lü, H., Li, S., Fan, D., Wang, P., Geng, D., Kang, C.S., & Zhang, Z.
781 (2020). Soil moisture retrievals using L-band radiometry from variable angular ground-based

782 and airborne observations. *Remote Sensing of Environment*, 248, 111958

783 Zheng, D., Li, X., Wang, X., Wang, Z., Wen, J., van der Velde, R., Schwank, M., & Su, Z.
784 (2019). Sampling depth of L-band radiometer measurements of soil moisture and freeze-thaw
785 dynamics on the Tibetan Plateau. *Remote Sensing of Environment*, 226, 16-25

786 **List of figure captions**

787 Fig. 1 Illustrations of the tower-based experiment at Cora Lynn, Victoria, Australia, including
788 a) location map of the site; b) the tower carrying PPMR and PLMR; c) the four-step tower
789 rotation cycle; d) PPMR operating at 0.742-0.752 GHz; and e) PLMR operating at 1.401-1.425
790 GHz.

791 Fig. 2 Illustrations of the ground measurements, including a) station 126 monitoring soil
792 moisture, temperature, and rainfall evolution; b) a diagram showing the station installation; c)
793 soil surface roughness measurement with the pin-profiler; d) surface soil moisture
794 measurement using HDAS; and e) an example of vegetation destructive sampling.

795 Fig. 3 Photos before the germination (top row) and at the maturity (middle row) of wheat, and
796 diagrams of soil surface profiles (bottom row) of the four quadrants for the data used in this
797 paper. Quadrants 3 and 4 were plowed in one pass and had the same roughness structures but
798 with different orientations (perpendicular and parallel, respectively) relative to the tower look
799 direction.

800 Fig. 4 Collected data including a) TB observations at 6 am in Q1 as an example, with the data
801 gaps resulting from the tower being lowered due to high wind on those days; b) station time-
802 series soil moisture with HDAS measurements (boxplots); c) station time-series soil
803 temperature; and d) observed (boxplots) with fitted (black line) vegetation water content in

804 Q1 as an example. For clarity only the data collected from the top 3 sensors are plotted in b)
805 and c). Corresponding to the soil moisture evolutions of station 126 (in blue) in Q2 and station
806 127 (in red) in Q1, 3 and 4, the blue and red boxplots in b) show the maximum, 75% percentile,
807 median, 25% percentile, and minimum of the spatial HDAS measurements in Q2 as well as
808 Q1, 3 and 4, respectively.

809 Fig. 5 RMSE (K) between the observed and simulated TB using a range of H_R values at H-
810 pol (top row) and V-pol (bottom row) over the bare soil in each quadrant. The model for bare
811 soil (Eq. 3) was adopted as the forward model. The dots with values indicate the minimum
812 RMSE and the corresponding H_R values for P-band (in blue) and L-band (in orange). The
813 parameters Q_R and N_{RP} were assumed to be the same as in the SMAP SCA at both P- and L-
814 band, being 0 and 2, respectively.

815 Fig. 6 Retrieved versus observed soil moisture for H-pol (top row) and V-pol (bottom row)
816 over the bare soil in each quadrant, using the SCA (Eq. 10) with the bare soil forward model
817 (Eq. 3). Calibrated H_R values from the period of bare flat soil in Q2 were used for all quadrants
818 here, i.e., 0.125 and 0.171 for P-band H- and V-pol, respectively, and 0.327 and 0.081 for L-
819 band H- and V-pol, respectively. The parameters Q_R and N_{RP} were assumed to be the same as
820 those from the SMAP SCA at both P- and L-band, being 0 and 2, respectively.

821 Fig. 7 Comparison of TB simulations against observations for H-pol (top row) and V-pol
822 (bottom row) over the wheat-covered soil in each quadrant, using the SCA (Eq. 10) with the
823 tau-omega model (Eq. 1). The default SMAP SCA parameters in Table 2 were used for all
824 quadrants, both bands, and both polarizations.

825 Fig. 8 RMSE (K) between the observed and simulated TB using a range of b and ω values for
826 P-band V-pol over the wheat-covered soil in each quadrant. The tau-omega model (Eq. 1) was
827 adopted as the forward model. The yellow circles indicate where the minimum RMSE was
828 reached, with the three values showing b , ω , and the minimum RMSE, respectively. The
829 calibrated H_R values at P-band V-pol from the period of bare soil, i.e., 0.174, 0.171, 0.070,
830 and 0.092, were used for Q1-Q4, respectively. The parameters Q_R and N_{RP} were assumed to
831 be the same as in the SMAP SCA, being 0 and 2, respectively.

832 Fig. 9 Observed versus retrieved soil moisture over the wheat-covered soil in each quadrant,
833 using the SCA-V (Eq. 10) with the tau-omega model (Eq. 1). The default SMAP SCA Q_R and
834 N_{RP} and the calibrated H_R , b , and ω parameters in Q2 (flat soil) were used for P-band in all
835 quadrants here, i.e., $Q_R = 0$, $N_{RP} = 2$, $H_R = 0.171$, $b = 0.099$, and $\omega = 0.134$. The default
836 SMAP SCA parameters in Table 2 were used for L-band in all quadrants.

837 Fig. 10 RMSE (K) between the observed and simulated dual-pol TB using a range of H_R and
838 Q_R values for P-band (top row) and L-band (bottom row) over the bare soil in each quadrant.
839 The model for bare soil (Eq. 3) was adopted as the forward model. The yellow circles indicate
840 where the minimum RMSE was reached, with the three values showing H_R , Q_R , and the
841 minimum RMSE, respectively. The N_{RP} was assumed to be 2, the same as in the SMAP DCA,
842 at both P- and L-band.

843 Fig. 11 Observed versus retrieved soil moisture over the wheat-covered soil in each quadrant,
844 using the DCA (Eq. 11) with the tau-omega model (Eq. 1). The default SMAP DCA N_{RP} and
845 ω were used for both P- and L-band, i.e., $N_{RP} = 2$ and $\omega = 0.06$. The calibrated H_R and Q_R

846 from the period of bare flat soil in Q2 were used for all quadrants, i.e., $H_R = 0.136$ and $Q_R = 0$
847 for P-band and $H_R = 0.231$ and $Q_R = 0.144$ for L-band.

848 Fig. 12 Observed versus retrieved soil moisture over the wheat-covered soil in Q2, using the
849 SCA-V (Eq. 10) with the bare soil forward model (Eq. 3). Calibrated H_R values from the period
850 of bare flat soil in Q2 were used here, i.e., 0.171 for P-band and 0.081 for L-band, while Q_R
851 and N_{RV} were assumed to be the same as those from the SMAP SCA at both P- and L-band,
852 being 0 and 2, respectively.